The Astronomical Journal, 134:77–95, 2007 July

AUTOMATED SELECTION AND CHARACTERIZATION OF EMISSION-LINE SOURCES IN ADVANCED CAMERA FOR SURVEYS WIDE FIELD CAMERA GRISM DATA

Gerhardt R. Meurer,[1] Z. I. Tsvetanov,[1] C. Gronwall,[2] P. Capak,[3] J. P. Blakeslee,[4] N. Benítez,[5] H. C. Ford,[1]
G. D. Illingworth,[6] L. D. Bradley,[1] N. Pirzkal,[7] J. Walsh,[8] R. J. Bouwens,[6] and S. Srinivasan[1]
Received 2006 May 30; accepted 2007 March 9

ABSTRACT

We present complementary techniques to find emission-line targets and measure their properties in a semi-automated fashion from grism observations obtained with the Advanced Camera for Surveys aboard the *Hubble Space Telescope* (*HST*). The first technique is to find all likely sources in a direct image, extract their spectra, and search them for emission lines. The second method is to look for emission-line sources as compact structures in an unsharp masked version of the grism image. Using these methods we identify 46 emission-line targets in the Hubble Deep Field–North using a modest (three-orbit) expenditure of *HST* observing time. Grism spectroscopy is a powerful tool for efficiently identifying interesting low-luminosity, moderate-redshift emission-line field galaxies. The sources found here have a median *i*-band (F775W) flux 1.5 mag fainter than the spectroscopic redshift catalog of Cohen et al. They have redshift $z \leq 1.42$, and high equivalent widths (typically >100 Å) and are usually less luminous than the characteristic luminosity at the same redshift. The chief obstacle in interpreting the results is line identification, since the majority of sources have a single emission line and the spectral resolution is low. Photometric redshifts are useful for providing a first-guess redshift. However, even at the depth of the state-of-the-art ground-based and *HST* data used here, photometric errors can result in uncertainties in line identifications, especially for sources with *i* magnitudes fainter than 24.5 ABmag. Reliable line identification for the faintest emission-line galaxies requires additional ground-based spectroscopy for confirmation. Of particular concern are the faint high-EW [O II] emitters, which could represent a strongly evolving galaxy population if the possibility that they are misidentified lower redshift interlopers can be ruled out.

Key words: galaxies: distances and redshifts — galaxies: high-redshift — methods: data analysis — surveys — techniques: spectroscopic

Online material: color figures

1. INTRODUCTION

One of the perennial problems in modern astrophysics is measuring spectral information, especially redshifts, of the most distant and hence faintest sources in the universe. With the *Hubble Space Telescope* (*HST*) and the Advanced Camera for Surveys (ACS) Wide Field Camera (WFC) astronomers can now obtain reliable broadband photometry down to ABmag ~ 27 across the optical portion of the spectrum with a modest expenditure of telescope time (e.g., Benítez et al. 2004). The instrument is able to image even deeper as demonstrated by the Hubble Ultra Deep Field (HUDF; Beckwith et al. 2006), which has a signal-to-noise ratio (S/N) of S/N = 10 limit of ~29.9 ABmag for point sources with the F775W filter (Bouwens et al. 2006); in the same field and using the same filter the S/N = 10 detection limit for extended sources within an aperture having diameter of 0.4″ and 0.5″ is 29.4 and 29.0 ABmag, respectively (Beckwith et al. 2006; Coe et al. 2006). However, our limit for obtaining reliable spectroscopy is much brighter. Spectra to ABmag ≈ 24 are difficult to obtain even with the largest ground-based telescopes (e.g., Abraham et al. 2004; Cowie et al. 2004; Cohen et al. 2000). At issue is the domination of the sky over the signal from astronomical sources observed from the ground at these faint magnitudes. The background seen by *HST* is orders of magnitude weaker. However, slit-survey spectroscopy with the now-defunct STIS and FOS spectrographs was not feasible due to the telescope's small aperture and minuscule projected slit widths. Alternatively, multiobject slitless spectroscopy is and has been available with *HST* using a variety of instruments (FOC, STIS, and NICMOS). All three cameras of ACS also have dispersing elements. The combination of the ACS G800L grism and the WFC is particularly noteworthy since it provides the widest field and highest throughput of all the slitless options on *HST*, allowing deep low-resolution spectroscopy with modest expenditure of telescope time. For example, the three-orbit integration of the Hubble Deep Field–North (HDF-N) that we discuss here provides S/N ~ 10 spectra in the continuum of sources having ABmag = 25.1 at a mean wavelength $\lambda \approx 8000$ Å.

While this major new capability is welcomed, grism data are difficult to work with. The broad spectral coverage of G800L ($\lambda = 5600$–9900 Å at 25% of peak spectral throughput; Walsh & Pirzkal 2005) results in a background count rate that is high compared to other WFC filters and indicates that wavelength variations in the flat field are a major concern. While the grism transmits most of its light in the first order, light from other orders of bright

---

[1] Department of Physics and Astronomy, Johns Hopkins University, Baltimore, MD 21218, USA.

[2] Department of Astronomy and Astrophysics, Pennsylvania State University, University Park, PA 16802, USA.

[3] Department of Astronomy, California Institute of Technology, Pasadena, CA 91125, USA.

[4] Department of Physics and Astronomy, Washington State University, Pullman, WA 99164, USA.

[5] Instituto Astrofísica de Andalucía (CSIC), Granada 18008, Spain.

[6] UCO/Lick Observatory, University of California, Santa Cruz, CA 95064, USA.

[7] Space Telescope Science Institute, Baltimore, MD 21218, USA.

[8] ESO Space Telescope European Coordinating Facility, D-85748 Garching bei München, Germany.

sources can also be seen. The orientation of the G800L filter and the strong geometric distortion of the ACS (Meurer et al. 2002) results in spectral traces that are skewed relative to the CCD pixel grid at an angle that varies across the field and a wavelength calibration that also is field dependent. The spatially varying distortion makes combining dithered G800L images difficult, especially if there are large offsets or roll-angle variations. Fortunately, astronomers at the Space Telescope European Coordinating Facility (ST-ECF) have provided calibrations of the G800L grism (Pasquali et al. 2003; Walsh & Pirzkal 2005), as well as the aXe software package for extracting and processing slitless spectra (Pirzkal et al. 2001), which relieves many of the pains of dealing with grism data.

The aim of this paper is to assess techniques to process grism data and identify emission-line galaxies (ELGs). ELGs are particularly interesting since they mark the location of AGNs or intense star formation and, hence, cosmic evolution. For example, some of the most distant galaxies in the universe are Lyα emission sources at $z \sim 6.6$ (Kodaira et al. 2003; Taniguchi et al. 2005; Kashikawa et al. 2006). In addition, sharp narrow emission features should be one of the easiest spectral signatures to find in grism data. Since this is primarily a techniques paper, our science analysis is relatively light, and includes basic comparisons of the key measurable properties of the ELGs (luminosity, equivalent width, and color) with other galaxy samples at a similar redshift. This analysis is sufficient to show that the grism provides an efficient means for selecting statistically significant samples out to $z \sim 1.5$. This study is similar to Pirzkal et al. (2004), which provided a detailed description of how the Grism ACS Program for Extragalactic Science (GRAPES) collaboration have reduced their G800L observations of the HUDF and extracted source spectra. Xu et al. (2007) presented their technique for identifying ELGs and the resulting catalog of sources found, while Pirzkal et al. (2006) discussed the morphology of these ELGs. Here we discuss WFC grism processing methods and tools that were developed by the ACS Science Team largely independently from the ST-ECF and GRAPES efforts and optimized for the discovery of ELGs. We apply these methods to observations of the HDF-N. A brief summary of this work was presented at the 2005 *HST* Calibration Workshop (Meurer 2006).

In § 2 we compare our data processing to that of the GRAPES collaboration and describe in detail our data and its processing. In § 3 we present two methods for finding ELGs, as well as our methods for assigning line identifications. Section 4 presents our results, including a list of all ELGs found and an initial assessment of the statistical properties of the galaxies found. In § 5 we compare our redshifts with other observations of the HDF-N and determine the redshift accuracy of the grism. Finally, in § 6 we summarize our results and discuss the benefits of using the grism and the additional requirements for obtaining useful redshifts of ELGs.

2. METHODS AND DATA

Here we provide an overview of our image processing and object extraction and note how it differs from that of the GRAPES collaboration (Pirzkal et al. 2004). Following that, we describe the processing of the HDF-N data in detail.

2.1. *Comparison of Image-Processing Techniques*

The GRAPES team do minimum processing of their images before extracting spectra. Like us, they rely on the STScI calibration pipeline CALACS (Hack 1999), as implemented by the STScI archive to do most of the basic CCD processing, consisting of overscan subtraction, bias subtraction, dark subtraction, and gain correction. These steps are performed using the best available reference files as implemented by the STScI archive. The flat field employed by CALACS for G800L images is a unity flat, so in effect no pixel-to-pixel flat-fielding is done. The GRAPES team subtracted a scaled supersky frame from each image to remove the sky background (where the scaling is to object free regions of the image). The G800L image shifts are determined from MULTIDRIZZLE-processed short exposures obtained through a broadband filter at the start of each orbit. The MULTIDRIZZLE task is also used to produce geometrically corrected G800L images, using the now-standard *drizzle* algorithm (Hook & Fruchter 1997; Koekemoer et al. 2002), but they are used only to identify the cosmic rays, not for spectral extractions. Instead, the extractions are performed by aXe on the individual frames after sky subtraction and masking of the cosmic rays. The spectra are co-added and the flat-fielding is performed at this stage by calculating the effective wavelength of the light falling on each pixel and interpolating between a series of broadband and narrowband flats (Walsh & Pirzkal 2005).

Our approach differs in a few key ways. First, we flat-field our G800L images with the flight flat-field for the F814W filter. We then process the data with the GTO science pipeline Apsis (Blakeslee et al. 2003a) to make cosmic-ray-rejected, aligned, combined, and geometrically corrected images. The result is one final G800L image, which we use to extract spectra and all spectroscopic quantities. There are several advantages of this approach. Application of the F814W flat cosmetically improves the images by largely removing most small-scale CCD blemishes. In addition, it produces flatter images, reducing the rms amplitude of the sky background over large scales ($\gtrsim 75$ pixels) by a factor of 2, as determined from application of the flat-field to the supersky frames used by Pirzkal et al. (2004). Since we forgo the use of aXe's λ dependent flat-field fit, the flux scale varies throughout the field of our images by up to $\sim 10\%$ (Walsh & Pirzkal 2005). Flat-field images from WFC show numerous dark blemishes that are more apparent with decreasing λ (Bohlin et al. 2001). Because of the broad spectral response of the grism, blemishes are inaccurately removed with the F814W flat. For example, if the blue end of the spectrum of a compact source falls on a blemish, it will not be completely removed by flat-fielding and result in a spurious absorption feature. However, this is not a major concern here since we are concerned with emission lines rather than absorption features. This is also less of a problem for extended sources ($\gtrsim 10$ pixels); since many wavelengths contribute to each pixel in the spectrum one can no longer assume that a single wavelength dominates, and hence our flat-fielding technique should be sufficient in these instances. Using small dithers can also mitigate against this happening. Combining geometrically corrected dithered data can work as long as there are no roll-angle variations and the dithers are all within $\sim 6''$. Then, the λ scales of the first-order spectra will align to within $0.025''$ (~ 0.5 WFC pixels) across the WFC field. Geometric correction has the advantage that it removes much of (but not all of) the spatial variation in the λ calibration with the dispersion remaining nearly constant within each spectrum. A major advantage of our approach is that the geometrically corrected spectra are nearly horizontal. Over a spectral length of 75 pixels, we calculate a slope of 0.03 pixels averaged over the geometrically corrected image (maximum slope of 0.99 pixels), while the average slope in the raw images is 2.54 pixels (maximum 3.43 pixels). Horizontal spectra are easier to extract and analyze using a variety of tools. The orientation also allows simple filtering to remove cross-dispersion structure and isolate emission lines (e.g., § 3.2). Finally, Apsis processing of the images provides excellent cosmic-ray and hot-pixel removal and removes a small amplifier step (typically having an amplitude of a few electrons) often seen in WFC images.

TABLE 1
HDF-N Observations

Filter	Exp. Time	N_{exp}	Resolution (pixels)
G800L	6870	6	2.14
F775W	4500	4	1.72
F850LP	6800	6	1.83

2.2. *The Data*

The HDF-N field (R.A. = $12^{\mathrm{h}}36^{\mathrm{m}}47.11^{\mathrm{s}}$, decl. = $+62°13'11.9''$) was observed by the ACS science team (program number 9301) for two orbits in the F775W (i_{775}) filter and three orbits with the F850LP (z_{850}) filter and G800L grism as summarized in Table 1. Two exposures per orbit were obtained in order to facilitate cosmic-ray removal, and the telescope was dithered by 1 pixel in each axis between orbits. The individual CALACS processed G800L "FLT" frames were divided by the standard F814W flat-field image. Fine alignment of the individual images was performed with Apsis. Apsis combined the individual exposures to make a single aligned image for each filter, F775W, F850LP, and G800L, using a spatial sampling of $0.05''$ pixel^{-1}, as well as a detection image that is the inverse sky variance weighted sum of the F775W and F850LP images. Because most objects in grism images are rather elongated and faint, Apsis could not accurately register the G800L FLT images and determine the offsets. Instead it employed default shifts determined from the positions that are stored in the image headers. We used a modified version of Apsis to check the shifts in the G800L "CRJ" images from the STScI CALACS pipeline; these are pairs of images combined to form a single cosmic-ray-rejected image. There are three CRJ images for this data set (one for each G800L orbit). Apsis matched 8–10 zero-order images of bright sources compared to the reference G800L CRJ image, yielding average shifts accurate to $\sim$0.05 pixels in each axis. The resulting shifts matched the default shifts to 0.1 pixels. The final Apsis drizzle cycle was done to an output scale of $0.05''$ pixel^{-1} with interpolation performed using a Lanczos3 kernel. The Lanczos3 function, defined by Mei et al. (2005), is a damped-sinc function. Application of it during drizzling results in better preservation of the noise characteristics and spatial resolution of the data than the standard linear (square) interpolation kernel (Mei et al. 2005). The FWHM resolution of the final F775W and F850LP images was measured from direct measurement of stellar radial profiles and reported in Table 1. For the G800L image we measure the spectral resolution from cross-dispersion cuts (five column sums) of the first-order spectra of stars. These were fitted with a Gaussian profile, and the resolution was taken to be the average FWHM of the fits. The resulting resolution of 2.1 pixels corresponds to $R \equiv \lambda/\Delta\lambda \approx 90$ at $\lambda = 8500$ Å at the center of the field.

We used the flux calibration curve given in Walsh & Pirzkal (2005) to convert spectra to flux units. As noted above, there is a $\sim$10% variation in the flux scale across the field when applied to data processed outside of the standard aXe extractions from FLT frames. We employed a λ calibration determined from WFC G800L images of Wolf-Rayet stars (which have strong bright emission lines) that were observed so as to fall on various positions on the WFC detector. The data and measurement techniques employed are identical to those used by Pasquali et al. (2003) but applied to the calibration data after drizzling them onto a rectified pixel grid with an output pixel scale of $0.05''$, the same as our data. The resulting λ calibration is given as a quadratic polynomial as a function of column offset from the geometrically corrected direct image, with the polynomial's coefficients varying quadratically with position in the corrected direct images.

3. FINDING EMISSION-LINE GALAXIES

We have developed two methods for the semiautomated identification and classification of ELGs, which we detail here. Here we define the term "emission-line galaxy" to be a galaxy having line emission detected in our grism images. In principle, line emission in an ELG may be dispersed evenly throughout the galaxy. In practice, it is usually confined to a small region, such as a nucleus or a knot. We use the term "emission-line source" (ELS) to denote a source of line emission that is distinct in position and wavelength. Effectively, an ELS can be isolated as a distinct source in the grism image. Hence, an ELG with two knots each with only one detected line has two ELSs. However, if each of its knots has two distinct lines then there are four ELSs in the system.

3.1. *Method A: aXe Selection*

Method A (for aXe) is very similar to that employed by the GRAPES team (Pirzkal et al. 2004; Xu et al. 2007). The extractions are done using aXe with the calibrations discussed above (§ 2.2) encoded into its configuration file. The extractions are done from the Apsis processed G800L image, which has a low-order sky background subtracted from it. No additional sky subtraction was performed. The aXe input catalog was derived from a SExtractor (Bertin & Arnouts 1996) catalog of the detection image. Since we are starting with spectra of entire galaxies (and stars), any line emission we find can be attributed to the galaxy as a whole (making it an ELG) but not localized further. However, multiple ELSs can be discerned within an ELG if there is more than one emission line. We configured aXe to extract spectra down to the detection limit $\sim$28.7 ABmag in the detection image. We go this faint to maximize the chance that we find faint "pure" ELGs, galaxies that have one emission line and no continuum. The grism observations have a similar exposure time and system throughput as the direct images; hence, a pure ELG will have similar count rates in the direct and grism images. Taking the differing exposure times and the rms noise level of the sky into account we calculate that the S/N ratio of a pure ELG would be similar in our detection and grism images. We caution that this condition may not hold for other data sets.

The detection image catalog was processed to remove sources with $m > 28.7$ ABmag (too faint) and semiminor axis size $b < 0.8$ pixels (too small, most likely image defects); aXe was configured to set the extraction aperture equal to 2.5 times the projected semimajor axis size a of the objects. However, first we reset the size of sources having $a < 2$ pixels or $25.4 < m \leq 28.7$ ABmag to $a = 2$, $b = 2$ pixels. Hence, our smallest extraction aperture is 5 pixels wide. The final step before extracting the spectra was to mask the area within 8 pixels of the edges of the CCD chips in the grism image due to the number of false positives we found in preliminary runs with our code.

One-dimensional flux-calibrated spectra were extracted with aXe. Automatic identification of "interesting" targets (ELG candidates) was performed by subtracting a smooth baseline spectrum and finding the sources with residuals having a peak $S/N \geq 4$. The baseline was constructed by median filtering the spectrum and then boxcar smoothing it, using a filter size of 19 pixels in both steps. The spectrum of each candidate was displayed and classified as either (1) an ELG, in which case one or more Gaussian components were fitted to the peak(s) in the spectrum; (2) a "star," that is, a source with strong broad absorption lines; our algorithm often mistakenly identifies the peaks between the absorption features as emission lines (the absorption lines sources are typically late-type M or K stars, although we also found the two supernovae discussed by Blakeslee et al. [2003b]); or (3) a spurious source. The sources classified in this manner are discussed in § 4.

3.2. *Method B: Blind Grism Image Selection*

Method B (for blind selection) starts with the grism image and is designed to identify all detectable ELSs. It is a "blind" selection in the sense that we do not require the a priori knowledge of source positions to find the ELSs. We find this to be very useful for two reasons. First, the ELSs we find are often confined to nuclei, off-center starbursts, or strong H II regions. Normal aXe extraction, as in method A, may dilute the line signal with "unnecessary" continuum flux or report the incorrect λ for the line if it results from an off-center knot. This is because in aXe extractions the λ of each pixel depends on its offset from the major axis in the direct image; λ errors may then occur for knots offset from the major axis. Since the flux scale depends on λ, a flux error will also result. Second, method A cannot find all possible pure emission-line sources. A pure ELG that emits at $5600\ \text{Å} \lesssim \lambda \lesssim 7100\ \text{Å}$ will be invisible in our direct images since the filters we employ do not have significant sensitivity at these wavelengths. However, the grism does, and hence we may still hope to find such sources, if they exist, in our grism images.

Processing starts with high-pass filtering both the grism image and the detection image. This is accomplished by smoothing with a 13×3 median filter and then subtracting this smoothed image from the original. The long axis of the filter is parallel to the image rows, that is, very nearly parallel to the dispersion direction. The filtering effectively removes most of the continuum in the grism image and much of the low-frequency spatial structure of the detection image, leaving compact ELSs in the grism image and galaxy nuclei, bars, and knots in the direct images. The high-pass filtered grism images also contain the zero-order images, offset by ~ -115 columns from the direct images. These could be mistaken for ELSs. So, before searching for emission-line candidates we mask those that could contaminate our results. This is done by determining a linear coordinate transformation[9] between the detection image positions and that of the zero-order images, as well as a mean flux ratio. In terms of count rate, objects in the F775W or F850LP image are on average 32 or 21 times brighter, respectively, than their zero-order counterparts in the grism image. We apply the appropriate flux ratio to the detection image to locate pixels that would have a flux equal to or greater than the sky noise in their zero order. The coordinate transformation is used to determine their location in the grism image. This pixel distribution is grown by a radius of three pixels by convolving it with a circular top-hat function. The resulting masked pixels are set to 0.0 in the filtered grism image. The total usable area of the image is then 17,087,178 pixels or 11.87 arcmin^2. Using this masking, about 60 spurious sources are excluded from the source catalogs (discussed below), while only 0.13% of the otherwise good area of the image is masked out. Hence, the masking is very efficient at removing spurious sources yet unlikely to remove many real ELSs from the grism image. Zero-order images may survive near the image edges where the direct image falls outside the field of view of our detection image. This condition is easily tested. Stars and very compact sources also remain in the high-pass filtered images because they are sharper than the smoothing box cross-dispersion width. However, they are easily recognized and flagged in the classification stage.

We use SExtractor to find sources in the masked and filtered grism image. By experimentation, we found that setting SExtractor parameters DETECT_THRESH and ANALYSIS_THRESH to 1.15 and DETECT_MINAREA to 3 was sufficient to find most obvious compact line emitters visible by eye without introducing large numbers of spurious detections. We removed from this catalog sources with output parameters ELONGATION (axial ratio) greater than 2.5 (likely spectral continuum residuals), B_IMAGE less than 0.4 or FWHM_IMAGE less than 1 pixel (likely residual cosmic rays or hot pixels), or FWHM_IMAGE greater than 7 pixels (spurious since sources this large should have been missing from the high-pass filtered images). For each source we extract a region extending from -150 to $+10$ columns from its position in the grism image and having an extraction width Δy rows equal to 1.25 times its size projected onto the cross-dispersion axis,

$$\Delta y = 1.25\sqrt{(a \sin\theta)^2 + (b \cos\theta)^2}. \tag{1}$$

Here a and b are the semimajor and semiminor axes A_IMAGE and B_IMAGE from SExtractor and θ is the position angle measured counterclockwise from the $+x$-axis defined as having constant row number in the pixel grid and directed toward increasing column number. The $+x$-axis is close to but not exactly the dispersion axis directed toward increasing wavelength. We set a minimum $\Delta y = 5$ rows for the extraction. This region is extracted from both the grism and direct filtered images, and the rows are then summed to make one-dimensional cuts. The region outside of a 13 pixel box centered on the emission line is set to 0.0 in the grism cut to isolate the ELS. The grism and direct cuts are then cross-correlated to determine the x offset between the ELS and sources in the direct image. If the cross-correlation peak corresponds to the correct source in the direct image, then the x offset yields the source position in the direct images and, hence, a preliminary estimate of the wavelength of the line.

Final measurements of the emission-line quantities are obtained from one-dimensional spectra of each knot extracted with aXe using the cross-correlation-determined position and an extraction aperture of 5 pixels. The emission-line properties are measured with Gaussian fits, as in § 3.1. However, we use a peak $S/N = 3$ cut, lower than that employed by method A, since we find that method B can (usually) reliably find ELSs at this low of a significance level. Comparison of the fluxes of 19 single-knot ELSs found by both methods show that lines are on average 0.04 dex brighter (with a dispersion of 0.14 dex) when measured with method A compared to B. We consider this not to be a significant difference.

Figure 1 shows an example of the image manipulation and detection process for this method. Since there are a number of ways this method can produce spurious results, this technique is applied in an interactive environment. For each candidate ELS, the cutouts of the grism and direct images are examined and used to assess whether it corresponds to a blemish in one of the images or a star (like method A, this technique is also adept at finding compact broad absorption-line sources). Line plots of the one-dimensional cuts and the cross-correlation spectrum are produced, as is the autocorrelation of the high-pass filtered grism spectrum with itself. The peaks in the cross-correlation are fitted with Gaussian profiles until the residuals have no peaks with $S/N \lesssim 3$. If there is more than one Gaussian component in the fit, the correct match is interactively selected using the two-dimensional cutouts and line plots as a guide; an ELS typically corresponds to a high surface brightness compact nucleus or knot with its

---

[9] $X_{\rm out} = a + bX_{\rm in} + cY_{\rm in};\ Y_{\rm out} = d + eX_{\rm in} + fY_{\rm in}$.

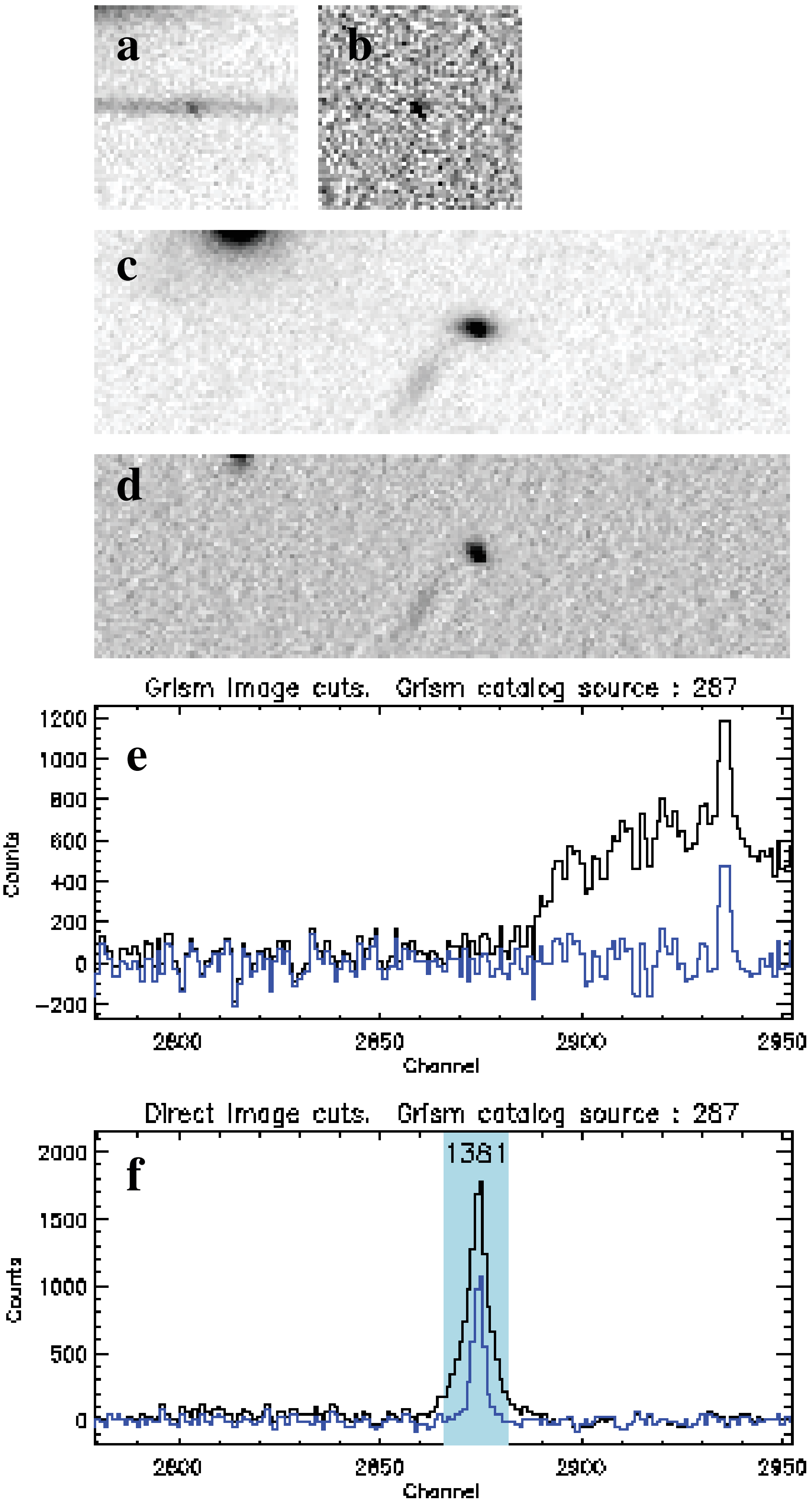

Fig. 1.—Steps in the processing of the grism and detection image for finding ELGs in the grism images and measuring their properties. Panels *a* and *b* show a 50 × 50 pixel cutout of the grism image before and after, respectively, subtracting a 13 × 3 pixel median filtered version of the image (high-pass filtering). These cutouts are centered on an emission-line candidate selected from the high-pass filtered grism image. Panels *c* and *d* show cutouts of the direct image before and after high-pass filtering. The width of the cutout is selected to include the full range over which the direct image counterpart to the source seen in panel *b* may reside. Panel *e* shows the one-dimensional spectra made by extracting and summing five rows centered on the emission line from the grism image before (*black line*) and after (*blue line*) high-pass filtering. Panel *f* shows the same thing for the one-dimensional cuts through the direct image. The shaded regions show the pixels in the collapsed region that belong to an object found by SExtractor (the working object identification number is shown).

two-dimensional line image resembling the high-pass filtered grism image in size and orientation. Spurious peaks in the cross-correlation typically can be identified (by eye) as having the wrong cross-dispersion position or not corresponding to a nucleus or knot. There remain cases, however, of more than one plausible direct counterpart to the ELS. This could be due to multiple knots in the direct image or completely separate sources. We flag these ambiguous cases. The sources classified by this technique are discussed in § 4.

3.3. *Line Identification and Redshift*

Two emission lines are found in seven ELGs, allowing line identification and redshifts to be determined using the ratio of observed wavelengths, which is invariant with redshift. In three cases the two lines are rather close and clearly correspond to Hβ and the [O III] $\lambda\lambda$4959, 5007 doublet, which is blended at the grism's resolution. In two cases the ratio of wavelengths indicates that the lines are Hα and [O III]. Note that one must be careful with this technique since $\lambda_{\mathrm{H}\alpha}/\lambda_{[\mathrm{O\,III}]} = 1.3138$ is close to $\lambda_{\mathrm{H}\beta}/\lambda_{[\mathrm{O\,II}]} = 1.3041$. A 1 pixel uncertainty in both line wavelengths could result an ambiguous line identification over the redshift range of interest. Our adopted identification in these two cases corresponds to previous spectroscopic and photometric z estimates (see below), indicating that our identifications are correct. In one case we identify the lines as Hβ and Hγ at $z = 0.947$, while in the last case we identify [O II] and [Ne III] 3869 Å.

The vast majority (39 of 46) of ELGs found contain only a single detected line. Identification of this line is a primary, but difficult, task. The line may well be a blend at the low resolution of our data (e.g., Hα and [N II], the [O III] doublet, and the [O II] $\lambda\lambda$ 3726, 3728 doublet). Similarly, the resolution is not high enough to identify lines by profile shape (e.g., Lyα). For these sources, our approach is to use available redshifts as a first guess to each source's redshift and then determine which line identification agrees best with the guess.

We use four sources for the redshift guesses, one spectroscopic source and three photometric redshift sources. Multiple estimates are used to ensure that all grism sources have at least one first-guess redshift and as a consistency check to determine how resilient the line identification is to the first guess source. In addition, the different redshift sources represent different choices of strategies and investments in telescope time, labor, and resources that may be employed to obtain redshifts. We have four redshift sources that we now list with the number of matches to the 46 ELGs: (1) spectroscopic redshifts (z_{spec}) from the compilation of the Hawaii group (Cowie et al. 2004) (22 matches); (2) photometric redshifts (z_{phot}) from Capak (2004, hereafter C04), who used terrestrial U, B, V, R, I, z, and HK photometry and derived z_{phot} estimates from the BPZ code, version 1.99, described by Benítez (2000) (37 matches); (3) Fernández-Soto et al. (1999, hereafter FLY99), who used U_{300}, B_{450}, V_{606}, and I_{814} photometry that they measured from the HDF data of Williams et al. (1996), as well as ground-based J, H, and K photometry from Dickinson (1998), to derive their z_{phot} estimates (25 matches); and (4) our own z_{phot} estimates, which we derive from the online Great Observatories Origins Deep Survey (GOODS) B_{435}, V_{606}, i_{775}, and z_{850} ACS photometry (release r1.1z; Giavalisco et al. 2004) (43 matches). For the latter we employed the BPZ code, version 2.0 alpha, described by Benítez (2000), which reports results on up to three peaks in the z probability distribution. We assume that the emission lines seen are one of the following: Hα, the [O III] $\lambda\lambda$4959, 5007 doublet, the [O II] $\lambda\lambda$3726, 3729 doublet, or Lyα, for which we adopt rest-wavelengths in vacuum of $\lambda_0 = 6564.6$, 4996.5, 3728.7, and 1216 Å, respectively. We adopted intrinsic flux ratios of $F_{5007}/F_{4959} = 3.03$ for the [O III] doublet (set by quantum mechanics), and $F_{3728}/F_{3726} = 1.3$, corresponding to an electron density $n_e = 100$ cm^{-3} (near the low-density limit; Osterbrock 1989) for the [O II] doublet.

4. RESULTS

4.1. *Data Presentation*

Properties of the 53 ELSs in the 46 unique ELGs found by our techniques are listed in Table 2. Column (1) gives the ELG identification number. The sources are ordered by z_{grism}; larger identification numbers indicate higher redshifts. Column (2) gives a coordinate-based name, mostly from the GOODS-North (GOODS-N) r1.1z catalog. The remaining columns are explained in the table notes. Postage-stamp cutouts of the ELGs taken from the detection image are given in Figure 2. Two stamps are given for each source, one from the plain detection image and the other from the high-pass filtered detection image. The former is ideal for identifying the field, while the latter is well-suited to show knots and other sharp structures not always seen in the plain detection image. Comments on individual ELGs are given in the Appendix.

We found 32 ELSs in 30 ELGs using method A; two of these ELGs have two emission lines detected with method A. Method B reaped more ELSs, 49 in 39 unique ELGs. Five of these have two lines detected with method B. Two ELGs have two identified emission knots, and one has four emission-line knots. The object centers for the extracted spectra and the method of detection is indicated in the stamps: squares mark sources identified with method A, and circles mark sources from method B. The line identification corresponds to [O III] in 26 cases, [O II] in 13 cases, Hα in eight cases, Hβ in four cases, Hγ in one case, and [Ne III] λ3869 in one case. There were four candidate "pure" ELGs, apparent emission-line sources with no direct counterpart. However, careful examination of the grism image and noise maps produced in the drizzling process show that they are all probably imperfectly removed cosmic rays and hot pixels.

4.2. *Properties of Grism-selected ELGs*

Here we examine some basic measured properties of the sample. These include line wavelength, flux, and equivalent width, as well as continuum magnitudes, colors, and luminosities. Our intent is to give an overview of the properties of our sample, examine the extent to which they are set by selection effects, and contrast them with other distant galaxy samples. It is not an analysis of the astrophysics of the ELGs, nor do we address issues of cosmology and the evolution of galaxy populations, since the emphasis of this paper is on how to find ELGs.

Figure 3 compares the wavelength distribution of our sample with the grism sensitivity curve. The distributions from method A and method B selection are shown separately. Both distributions and the curve peak at similar λ and have a relatively long red tail. However, there is a deficit of detections of lines at $\lambda \lesssim 7000$ Å compared to the sensitivity curve. One-sided Kolmogorov-Smirnov tests yield probabilities of 7% and 3% that the observed λ distribution follows the grism sensitivity curves for method A and B selection, respectively. So while the sensitivity curve may play a significant role in determining which ELGs are selected, other factors, including the volumes accessed by the individual lines, the luminosity function, and large-scale structure also effect the λ distribution.

We compare our line flux distributions in Figure 4. The observed distributions are similar for the two selection techniques, although there is a hint that method B is finding more faint lines than A. The peak in the distributions is at $F_{\mathrm{line}} \approx 4 \times 10^{-17}$ ergs cm^{-2} s^{-1}.

TABLE 2
EMISSION-LINE SOURCES

ELG (1)	Name (2)	i_{775} (3)	$z_{\rm spec}$ (4)	$z_{\rm phot}$ (5)	Source (6)	$z_{\rm grism}$ (7)	ID (8)	EW (9)	$\log(F_{\rm line})$ (10)	Method (11)	Notes (12)
1	GOODSN J123641.63+621132.1	19.78	0.089	0.090	C	0.098	Hα	127	−15.52	BA	a
2	GOODSN J123644.75+621157.4	25.06	. . .	0.210	C	0.124	Hα	223	−16.43	B	b, c
3	GOODSN J123633.16+621344.0	25.31	. . .	0.220	C	0.126	Hα	155	−16.59	BA	c
4	GOODSN J123646.53+621407.9	23.95	0.130	0.160	C	0.128	Hα	115	−16.33	BA	
5	GOODSN J123648.30+621426.9	19.01	0.139	0.130	C	0.136	Hα	62	−15.52	BA	a
6	GOODSN J123651.72+621220.5	21.62	0.300	0.320	C	0.302	Hα	58	−16.20	BA	
7	GOODSN J123658.06+621300.8	22.45	0.319	0.310	C	0.308	Hβ	9	−16.68	B	d
							[O III]	8	−16.78	B	d
8	GOODSN J123626.57+621321.2	26.56	. . .	0.483	B	0.318	[O III]	6418	−16.68	A	c
9	GOODSN J123650.82+621256.3	22.61	0.319	0.310	C	0.319	[O III]	250	−16.00	B	a, d
							Hα	169	−16.30	B	d
10	GOODSN J123646.59+621157.5	25.77	. . .	0.440	C	0.341	[O III]	248	−16.44	BA	c
11	GOODSN J123653.10+621438.4	24.53	. . .	0.430	C	0.376	[O III]	123	−16.49	B	
12	GOODSN J123628.76+621335.8	25.99	. . .	0.559	B	0.427	[O III]	204	−16.56	BA	
13	ACS J123632.69+621239.1	23.15	0.458	0.420	C	0.433	[O III]	65	−16.46	B	
14	GOODSN J123637.56+621240.4	22.23	0.457	0.153	B	0.445	[O III]	12	−16.58	B	b
15	GOODSN J123637.64+621241.3	21.08	. . .	0.436	B	0.446	[O III]	81	−16.09	BA	d
							Hα	155	−15.99	B	d
16	GOODSN J123650.79+621221.7	24.71	. . .	0.440	C	0.450	[O III]	254	−16.27	BA	
17	GOODSN J123657.30+621300.0	21.40	0.473	0.420	C	0.465	[O III]	89	−16.41	B	
18	GOODSN J123644.19+621248.2	21.62	0.555	0.540	C	0.476	[O III]	20	−16.05	A	
19	GOODSN J123637.76+621235.6	23.86	. . .	0.480	C	0.477	[O III]	172	−16.36	B	
20	ACS J123636.58+621336.8	26.77	. . .	0.620	C	0.478	[O III]	315	−16.45	BA	c, e
21	GOODSN J123645.24+621108.9	23.41	0.513	0.580	C	0.505	[O III]	162	−16.14	BA	
22	GOODSN J123655.58+621400.3	24.17	0.559	0.590	C	0.551	[O III]	147	−16.44	BA	
23	GOODSN J123645.32+621143.2	23.85	0.557	0.570	C	0.552	[O III]	198	−16.15	BA	
24	ACS J123657.48+621212.0	23.29	. . .	0.720	F	0.555	[O III]	26	−16.59	BA	
25	GOODSN J123644.75+621144.1	24.87	. . .	0.670	C	0.562	[O III]	91	−16.54	B	
26	GOODSN J123654.39+621434.7	22.26	0.577	0.690	C	0.573	[O III]	13	−16.50	A	d
							Hβ	11	−16.54	A	d
27	GOODSN J123645.53+621330.2	25.38	. . .	0.540	C	0.670	[O III]	243	−16.47	BA	b, c
28	GOODSN J123636.47+621419.1	24.30	. . .	0.700	C	0.684	[O III]	341	−15.81	BA	d
							Hβ	115	−16.47	B	d
29	GOODSN J123646.96+621133.0	24.27	. . .	0.700	C	0.685	[O III]	198	−16.12	BA	
30	GOODSN J123647.24+621134.7	27.10	. . .	1.518	B	0.717	[O II]	121	−16.24	A	f
31	GOODSN J123629.72+621329.9	22.83	0.746	0.700	C	0.737	[O III]	28	−16.15	A	
32	GOODSN J123642.29+621429.9	23.77	. . .	0.850	C	0.841	[O III]	287	−16.04	B	
33	GOODSN J123644.17+621430.5	24.66	0.863	0.925	B	0.858	[O III]	175	−16.23	BA	b, c
34	GOODSN J123652.97+621257.1	25.63	. . .	0.800	F	0.943	[O II]	182	−16.32	BA	c
35	GOODSN J123636.63+621347.1	21.44	0.962	0.386	B	0.947	Hγ	7	−16.34	A	d
							Hβ	14	−16.07	A	d
36	GOODSN J123649.35+621155.4	23.41	0.961	1.115	B	0.954	[O II]	32	−16.39	BA	d
							[Ne III]	13	−16.81	B	d
37	GOODSN J123649.47+621456.9	24.11	0.341	0.970	C	1.003	[O II]	107	−16.69	B	b, g
38	GOODSN J123654.45+621152.8	24.40	. . .	1.040	C	1.017	[O II]	36	−16.63	B	
39	GOODSN J123658.30+621214.5	23.33	1.020	0.970	C	1.026	[O II]	40	−16.32	B	
40	GOODSN J123645.46+621357.3	26.17	. . .	0.920	F	1.073	[O II]	425	−16.37	BA	b
41	GOODSN J123643.42+621151.9	23.12	1.241	1.200	C	1.237	[O II]	22	−16.55	BA	
42	GOODSN J123653.51+621141.4	23.89	. . .	1.490	C	1.263	[O II]	46	−16.35	BA	b
43	GOODSN J123644.98+621240.0	24.07	. . .	1.170	C	1.337	[O II]	578	−16.20	A	
44	GOODSN J123652.77+621354.7	22.73	1.355	1.440	F	1.346	[O II]	41	−16.20	B	
45	GOODSN J123642.55+621150.3	24.97	. . .	1.600	C	1.422	[O II]	228	−16.57	B	b
46	GOODSN J123648.48+621120.7	26.87	. . .	1.141	B	1.424	[O II]	198	−16.49	B	c

NOTES.—Col. (1): ELG identification number (this work). Col. (2): Names preceded by GOODSN are the IAU specified name from the GOODS release r1.1z (Giavalisco et al. 2004). Names preceded by ACS could not be matched with the GOODSN catalog. Col. (3): SExtractor magnitudes of our images through the F775W filter in the ABmag system. Col. (4): Spectroscopic redshift $z_{\rm spec}$ taken from the Hawaii group compilation (Cowie et al. 2004). Cols. (5) and (6): The adopted photometric redshift $z_{\rm phot}$ and its source: C, C04; F, FLY99; and B, our own BPZ measurements using GOODS photometry. Entries in these two columns correspond to cases that do not match col. (7), the adopted grism redshift, $z_{\rm grism}$. Col. (8): Adopted line identification. Col. (9): Rest-frame equivalent width in Å. For the one case where $z_{\rm grism}$ is undefined, the observed EW is listed. Col. (10): The logarithm of the measured line flux in ergs $\rm cm^{-2}\ s^{-1}$. Col. (11): The methods that detected the line emission: A, aXe selection; B, blind grism selection. When a line is identified by both methods, then the data from cols. (7)–(9) are taken from method B. Col. (12): Notes: a, multiple line-emitting knots; b, $z_{\rm grism}$ differs depending on $z_{\rm phot}$ source; c, large $z_{\rm phot}$ errors result in ambiguous line ID; d, two lines identified; e, photometry not from GOODS release r1.1z, see individual object notes; f, no line identification allowed within $z_{\rm phot}$ error bars, nearest expected line chosen; g, $z_{\rm spec}$ and $z_{\rm grism}$ do not agree. Blank entries for cols. (1)–(7) occur for the second emission line in sources with two emission lines (note a). These blank entries thus have the same values as the previous line.

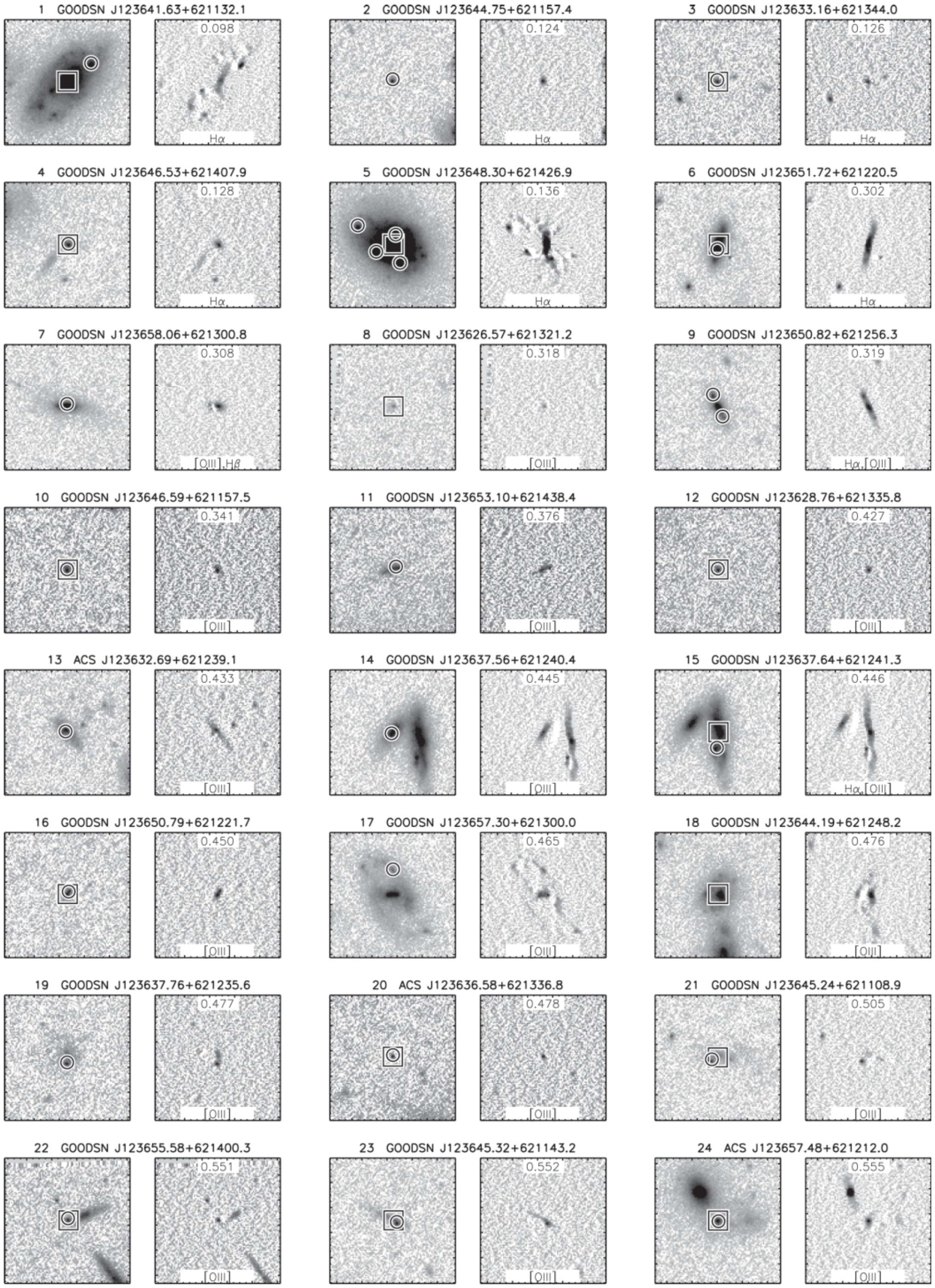

Fig. 2.—Postage stamp images, 5″ on a side, of the 46 ELGs, arranged by redshift. For each galaxy, two versions of the detection image are shown. The left panels show the detection image with spectrum extraction aperture locations containing emission lines marked: squares from method A, and circles from method B. The right panels shows the high-pass filtered detection image (see § 3.2 and Fig. 1). Here, the grism redshift is noted at the top of the panel, and the identified lines are noted at the bottom. The final panel shows the orientation of the images.

For comparison we show the $F_{\rm line}$ distribution from the STIS Parallel Survey (SPS; Teplitz et al. 2003a, 2003b). The SPS is similar to our survey in that it was obtained with *HST* using observations with a range of exposure times (typically a few thousand seconds, i.e., similar to that used here), albeit with an instrument, the STIS, that has a much smaller collecting area and lower throughput than our observing configuration. We see that our observations typically reach about 4 times deeper in line flux, probably because of the improved sensitivity. The peak in our $F_{\rm line}$ distributions corresponds to a 10 σ detection within a 5×5 pixel box for a line having λ at the peak of the sensitivity curve. However, the λ distribution is broad, and many lines are detected off the peak in the sensitivity curve (cf. Fig. 3). The distribution of measured S/N is shown as insets in Figure 4. The S/N histograms show that we start to lose lines at S/N $\lesssim 6$. As noted in §§ 3.1 and 3.2 our initial source selection requires a *peak* S/N = 4 and 3, respectively, in one-dimensional spectra. We are not finding weaker detections because here we are showing S/N measurements of *integrated* line flux within a 5×5 pixel box. One could dig further down in flux by convolving the one-dimensional spectra with a matched

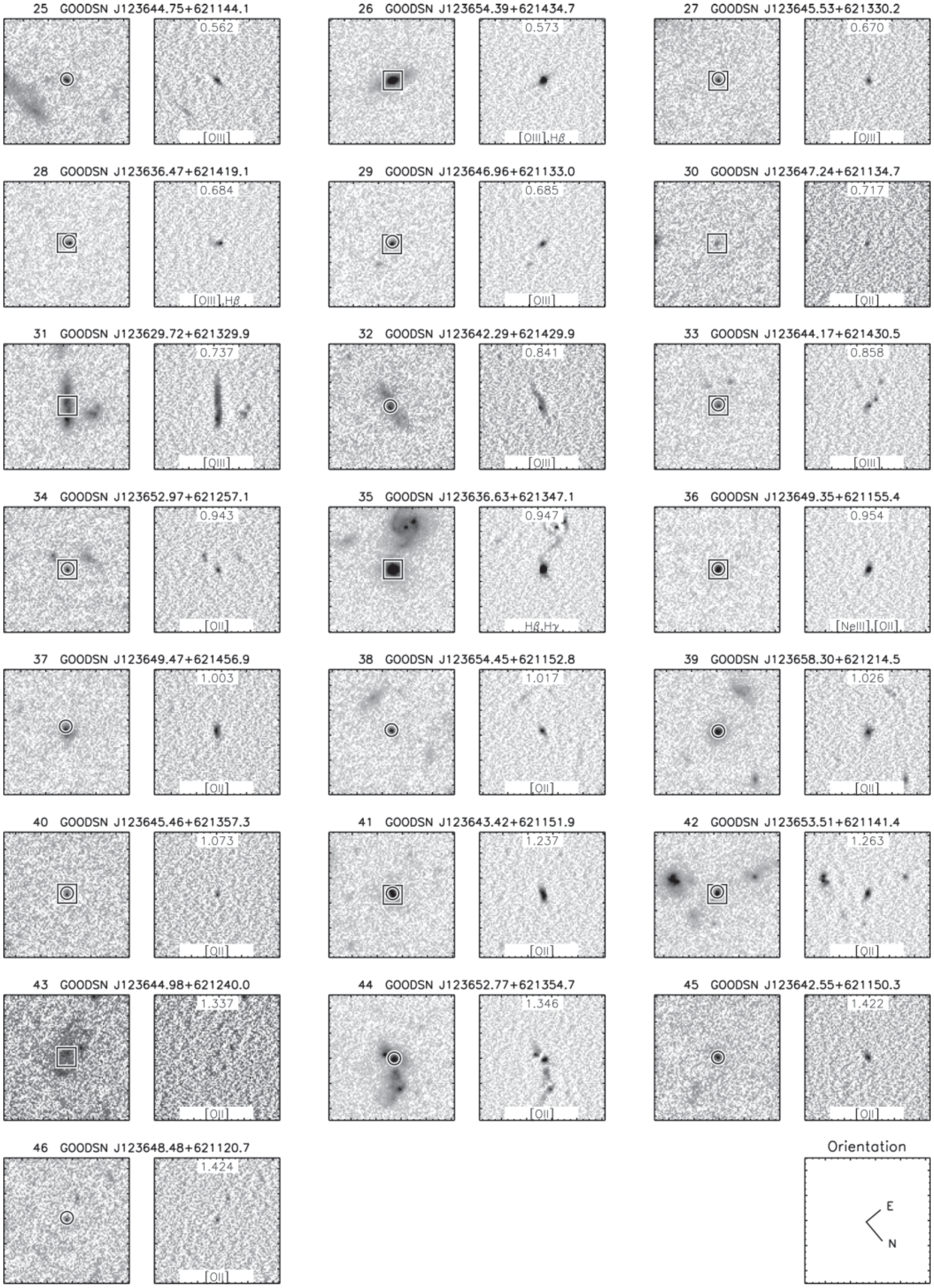

Fig. 2—*Continued*

filter and then lowering the peak S/N detection limit, although this would require weeding out more spurious sources.

Figure 5 shows the i_{775} magnitude distribution of the ELGs in comparison to two other samples in this field; the Hawaii group $z_{\rm spec}$ compilation of Cowie et al. (2004) and the $z_{\rm phot}$ catalog of C04. Only the sources that match sources in our detection image are included in the histograms to ensure that the comparison covers the same area on the sky. For the grism sample, the median i_{775} is 23.9 ABmag and the 75th percentile is $i_{775} = 24.9$ ABmag. These are significantly fainter than $i_{775} = 23.1$, and 23.8 ABmag, respectively, at these percentiles for the Hawaii $z_{\rm spec}$ compilation. Through expending considerable effort and time (particularly with the Keck telescopes) they were able to determine spectroscopic redshifts for over 4 times as many sources (210) than the number of ELGs we find. Nevertheless, with a modest three-orbit exposure we determined grism redshift estimates for 23 sources with no previous $z_{\rm spec}$ estimates.

The faint apparent magnitudes correspond to low luminosities compared to typical galaxies. This is shown in Figure 6, which plots histograms of absolute magnitude in the rest-frame B band, M_B, for our ELG sample, divided by line identification. We derived M_B by interpolating the broadband spectral energy distribution (SED) of the ELG host from the *HST* GOODS optical photometry (Giavalisco et al. 2004) to determine the apparent

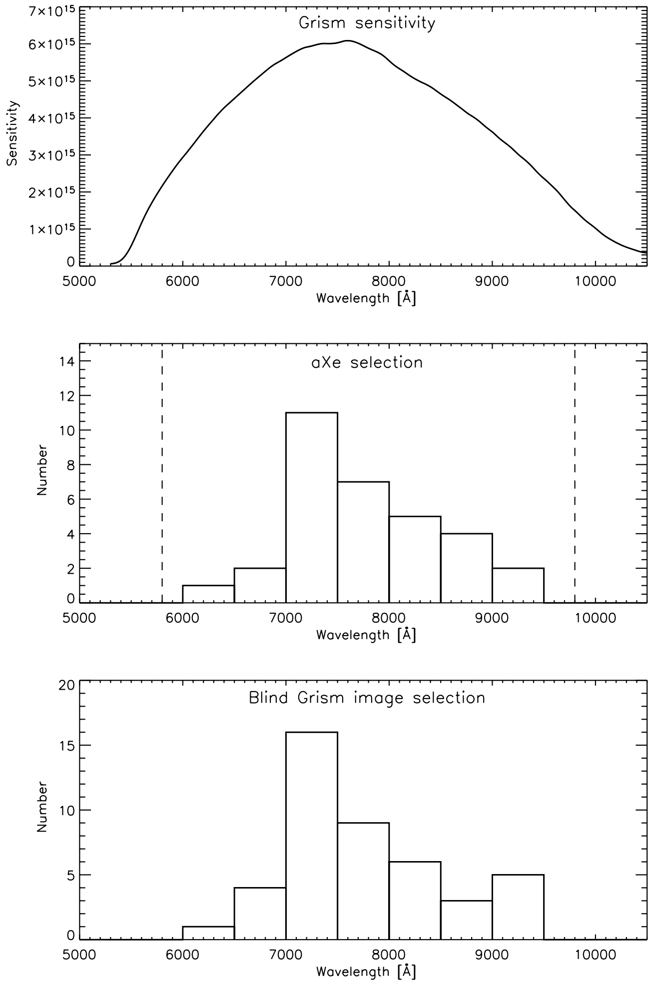

FIG. 3.—Comparison of the λ distribution of the lines found in the ELGs with the grism sensitivity curve. The grism sensitivity curve of Walsh & Pirzkal (2005) is shown in the top panel. The units of the ordinate are ergs cm^{-2} s^{-2} Å^{-1} DN^{-1}. The middle plot shows the histogram of λ values found with method A. The dashed lines delimit the λ search range for emission lines. The bottom panel shows the λ histogram for the method B–selected ELGs.

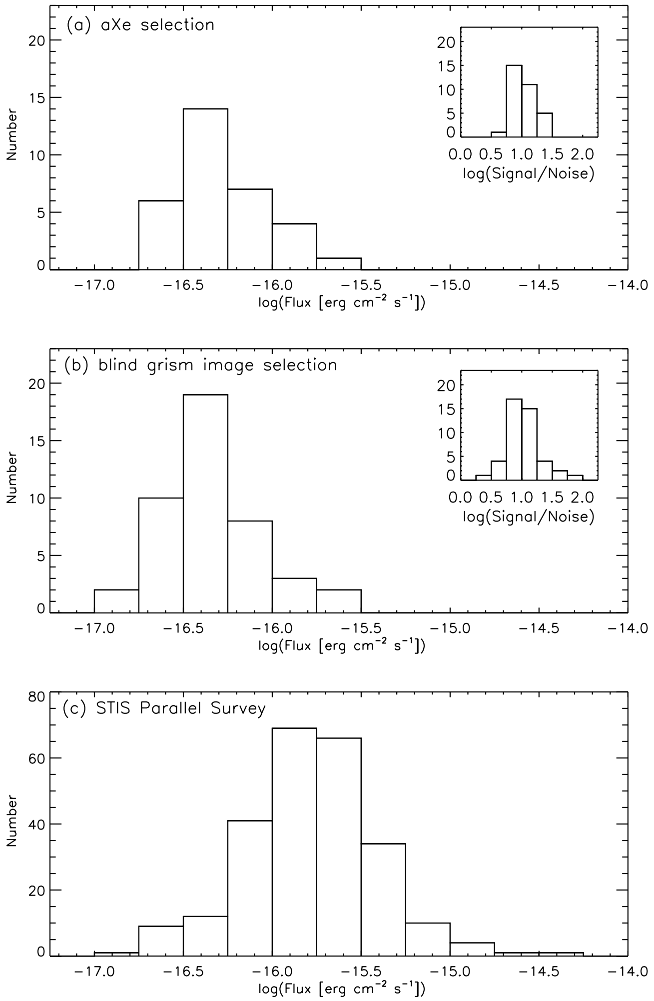

FIG. 4.—Line flux distribution of the ELSs found with (*a*) the direct image selection and (*b*) grism image selection compared to the ELSs found in the STIS Parallel Survey (*c*; Teplitz et al. 2003a). The inset in panels *a* and *b* shows the distribution of the line S/N.

ABmag at rest $\lambda_0 = 4297$ Å, the central λ of the B filter. We used the apparent magnitude in the nearest filter with data for cases where this λ in the observed domain falls outside the range of central wavelengths of the ACS filters used by GOODS. The absolute magnitude was then calculated for our adopted $z_{\rm grism}$ assuming $H_0 = 70$ km s^{-1} Mpc^{-1}, $\Omega_M = 0.3$, and $\Omega_\Lambda = 0.7$ (following Carroll et al. 1992). Table 3 presents the first quartile, median, and third quartile values of M_B and $z_{\rm grism}$ for our ELG sample, divided by emission-line identification (ID). We use a gray line to mark the absolute magnitude corresponding to $m = 27$ ABmag for an object at the redshift corresponding to the relevant line being found at $\lambda = 7500$ Å (the peak throughput of the grism). This gives a crude indication of the limiting magnitude for each type of line emitter. It is not an absolute limit, since less luminous sources are still possible, corresponding to finding somewhat fainter apparent magnitudes (see Fig. 5) or bluer lines (hence closer sources). For comparison, we also mark the characteristic absolute magnitude at the knee of the luminosity function, $M_B^\star$, derived from various galaxy surveys in the literature as vertical dotted, dashed, and dash-dotted lines in Figure 6. The galaxy surveys used were chosen to sample redshifts similar to the ELG samples and to be broadly representative of the field galaxy population. For the Hα-emitting ELGs we show $M_B^\star$ derived from the Sloan Digital Sky Survey (SDSS) luminosity function (Blanton et al. 2003; $M_B^\star = -20.31$) and the Two Degree Field Galaxy Redshift Survey (2dFGRS; Madgwick et al. 2002; $M_B^\star = -20.56$), while for the [O III] and [O II] emitters we use the K-band-selected rest-frame B-band GOODS luminosity-function results at $z = 0.46$ ($M_B^\star = -21.43$) and 0.97 ($M_B^\star = -21.45$), respectively (Dahlen et al. 2005).

In all cases the ELG samples have median M_B values below that of the field population at the same redshift. As one might expect, the difference between $M_B^\star$ and the median M_B of the ELGs depends on the redshift and, hence, the lines identified in our survey. There is an interesting difference in the histograms at the bright end. There are no Hα or [O III] emitters with $M_B < -21$, while seven of the 11 [O II] emitters are brighter than this value, with the most luminous, object 44, having $M_B = -23.5$. This difference may be due to sample size and relative volume: the volume available to [O II] emitters is 14 times that available to Hα emitters and 2.7 times that available to [O III] emitters. Hence, if the samples all had the same parent luminosity function, then the density of [O II] emitters implies that we might expect about three [O III] emitters with $M_B < -21$ in our survey. A larger sample is needed to determine if the apparent deficit of high-luminosity [O III] emitters is real. The surface density of the most luminous [O II] emitters is consistent with what we know about the luminosity

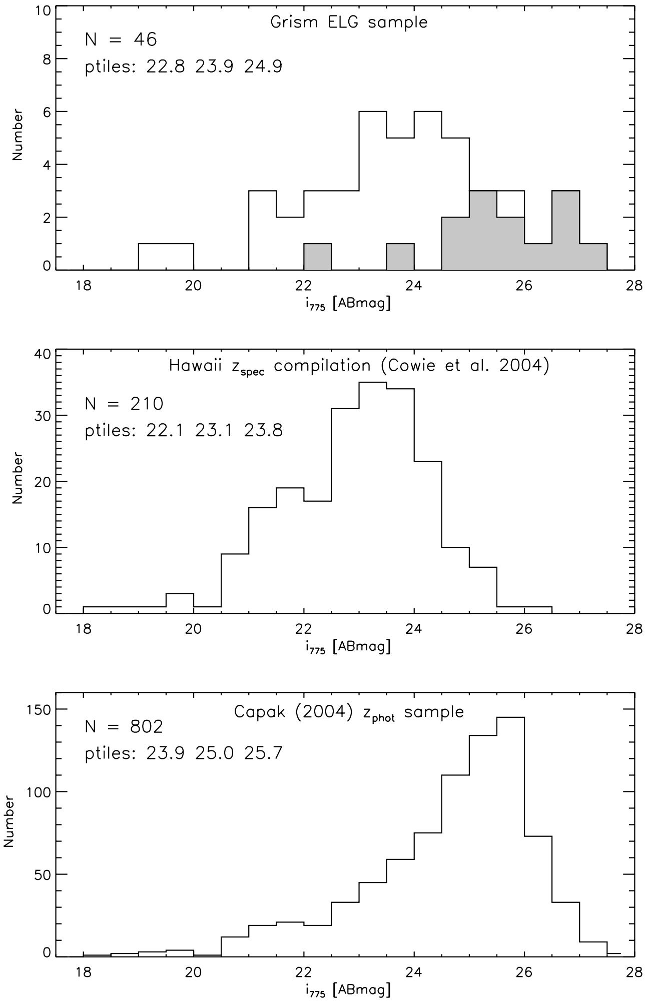

FIG. 5.—Histogram of i_{775} magnitudes of the grism-selected ELG sample (*top*) compared with the spectroscopic redshift sample of Cowie et al. (2004; *middle*) and the photometric redshift sample of C04 (*bottom*). Objects from the latter two samples are only included in the histograms if they match with sources cataloged in our detection image. All i_{775} magnitudes are derived from our ACS images. In the top left of each panel we report the total number of sources in the sample and the 25th, 50th (median), and 75th percentile i_{775} magnitudes. In the top panel sources with ambiguous $z_{\rm grism}$ estimates (notes d–g in Table 2) are indicated by the shaded histogram.

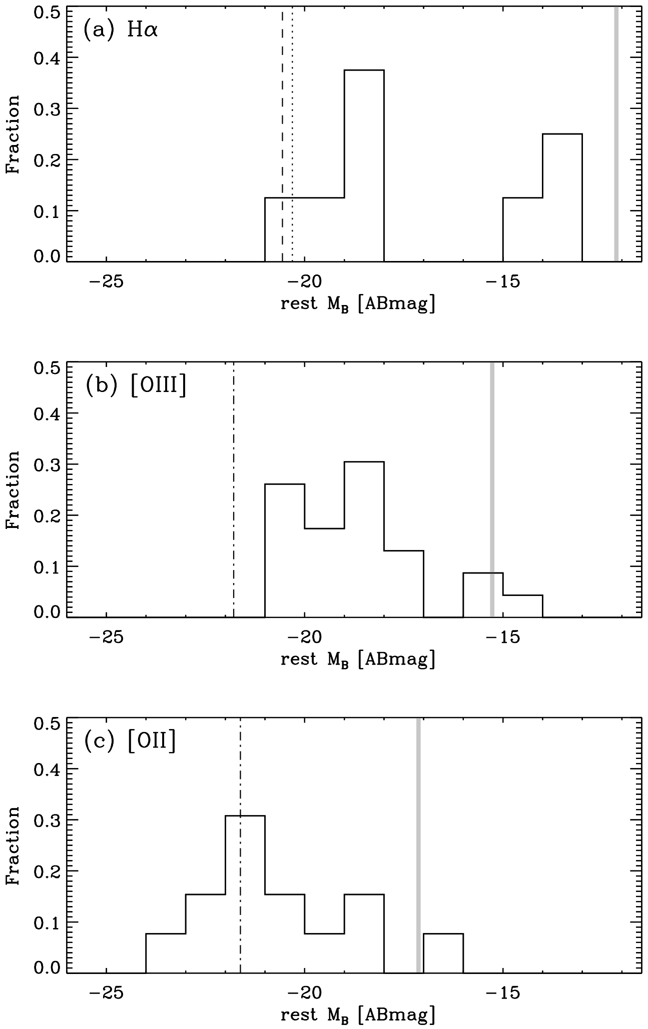

FIG. 6.—Rest-frame *B*-band absolute magnitude histograms of the ELGs split by line identification, showing galaxies detected in (*a*) Hα, (*b*) [O III], and (*c*) [O II]. The gray line shows the absolute magnitude corresponding to $m = 27$ ABmag for a line found at $\lambda = 7500$ Å; this is a crude estimate of the faintest galaxies we are likely to find. The other vertical lines indicate the knee of the luminosity function, M_B^* of field galaxies at similar redshift to the ELG samples. In panel *a* the dashed line shows M_B^* derived from the SDSS luminosity function (Blanton et al. 2003), while the dotted line shows the M_B^* of 2dFGRS (Madgwick et al. 2002). The mean $z \approx 0.1$ for both of these surveys. In panels *b* and *c* we show M_B^* derived from the *K*-band-selected GOODS luminosity function at a mean *z* of 0.46 and 0.97, respectively (Dahlen et al. 2005).

function at the redshifts we sample. For example, Dahlen et al. (2005) found that galaxies with $M_B < -22$ have a surface density of 0.37 arcmin^{-2} from a K_S-band selection in the GOODS-South field, while the three galaxies we find yield a surface density of 0.25 arcmin^{-2}.

The rest-frame equivalent width (EW) is effectively a measurement of the ionizing flux relative to the underlying continuum. The EW was calculated from the aXe spectra using

$$\mathrm{EW} = \frac{F_{\rm line}}{f_\lambda(1+z)}, \tag{2}$$

where f_λ is the continuum flux density, measured from the spectra. Caution must be used in interpreting EW values, especially at the high end, due to background subtraction uncertainties. For Hα, the EW gives an indication of the present star formation rate compared to the past average. The interpretation is less clear for the [O III] and [O II] EW. [O III] is considered a less reliable tracer of star formation because of its metallicity dependence, while the underlying continuum for [O II] emission is likely to be dominated by A stars, perhaps produced in the same event causing the [O II] emission.

Figure 7 shows the EW distribution of our sample compared to a variety of galaxy samples out to moderate redshifts. EW statistics of our sample, split by line ID, are compiled in Table 3, as are the corresponding statistics of the comparison samples. Figure 7*a* compares all the lines we measure to two local samples: ELGs found with prism spectroscopy by the KPNO International Spectroscopy Survey (KISS) red surveys (Salzer et al. 2001; Gronwall et al. 2004), and H I–selected ELGs imaged with narrowband filters for the Survey of Ionization in Neutral Gas Galaxies (SINGG; Meurer et al. 2006). The grism-selected ELGs have significantly higher EWs. The differences between the samples may largely be due to selection, measurement, or instrumentation differences. While both the KISS and our grism survey use slitless spectroscopy, the KISS survey has a higher dispersion

TABLE 3

Redshift, Absolute Magnitude, and EW Statistics of ELGs Split by Line Identification

Property	Hα	[O III]	[O II]
Grism-selected ELGs (this study)			
Number	8	23/26[a]	13
Redshift, z:			
Minimum	0.098	0.308	0.717
25th percentile	0.126	0.436	1.003
Median	0.132	0.478	1.073
75th percentile	0.306	0.570	1.337
Maximum	0.446	0.858	1.424
B-band absolute magnitude, M_B (ABmag):			
Minimum	−20.92	−20.97	−23.46
25th percentile	−18.97	−20.19	−21.87
Median	−18.29	−18.93	−21.27
75th percentile	−14.17	−18.00	−19.93
Maximum	−13.03	−14.32	−16.61
Rest-frame equivalent width, EW (Å):			
Minimum	58	8	22
25th percentile	102	69	40
Median	140	167	107
75th percentile	159	247	198
Maximum	223	6418	578
CFRS (Hammer et al. 1997)			
Number	95	175	270
Rest-frame equivalent width, EW (Å):			
Minimum	4	0.7	1.3
25th percentile	27	7	16
Median	41	15	27
75th percentile	63	28	39
Maximum	1520	1022	981
SPS (Teplitz et al. 2003a)			
Number	18	33	78
Rest-frame equivalent width, EW (Å):			
Minimum	19	13	6
25th percentile	75	55	45
Median	103	124	68
75th percentile	148	264	117
Maximum	394	1479	750

[a] There are 26 [O III] emitters; however, three are missing GOODS photometry (see Table 2). Therefore, we use the 23 sources with GOODS photometry to compile the M_B statistics, while all 26 sources are used to compile redshift and EW statistics.

(24 Å pixel^{-1}) and employs a filter that limits the spectral range to cover 800 Å, thus limiting the sky background. This makes it easier to detect lower EW systems. Because of the higher spatial resolution of our data, the ACS spectra have extraction aperture widths of typically 0.25″, more than an order of magnitude smaller than the 4″–5″ resolution of the KISS survey. This means that the continuum in the ACS grism spectra are less diluted by non–line-emitting portions of the host galaxy. The SINGG survey uses a totally different technique, narrowband images to isolate Hα and R-band images for continuum subtraction accurate to a few angstroms, allowing even lower EW values to be measured. Consequently, SINGG includes many low surface brightness and low EW systems.

Figures 7*b*–7*d* split our sample by line ID and compare the EW histograms to those from the Canada-France Redshift Survey (CFRS; Hammer et al. 1997) and SPS (Teplitz et al. 2003a, 2003b) for (*b*) Hα emission, (*c*) [O III] emission, and (*d*) [O II] emission. The CFRS is an *I*-band-selected terrestrial spectroscopic survey, while the SPS is a *HST* slitless spectroscopic survey of effectively random high-latitude fields. Both comparison samples have numerous detections of the three lines of interest and samples that extend out to $z \approx 1.5$. Our survey typically finds higher EW values for all lines than found in the CFRS. Again, this could in part be due to instrumentation differences; the CFRS spectra were obtained through 1.75″ wide slitlets (Le Fèvre et al. 1995), typically covering a large fraction of the galaxy and about an order of magnitude larger than the extraction apertures we use. The SPS data are closer in nature to ours. The STIS slitless spectral resolution is significantly finer than our data; the 2 pixel resolution element corresponds to ∼10 Å, allowing STIS to detect lower EW features. Despite that, the SPS EW distributions are broadly similar to ours. This suggests that the relatively high EWs seen by SPS and ourselves compared to the CFRS may result from the smaller projected aperture sizes afforded by the space-based observations.

We next consider the broadband optical colors of ELGs in order to assess whether they can easily be selected by color. The $B_{435} - i_{775}$ versus $i_{775} - z_{850}$ two-color diagram of the ELGs identified in this study are compared to all HDF-N galaxies in

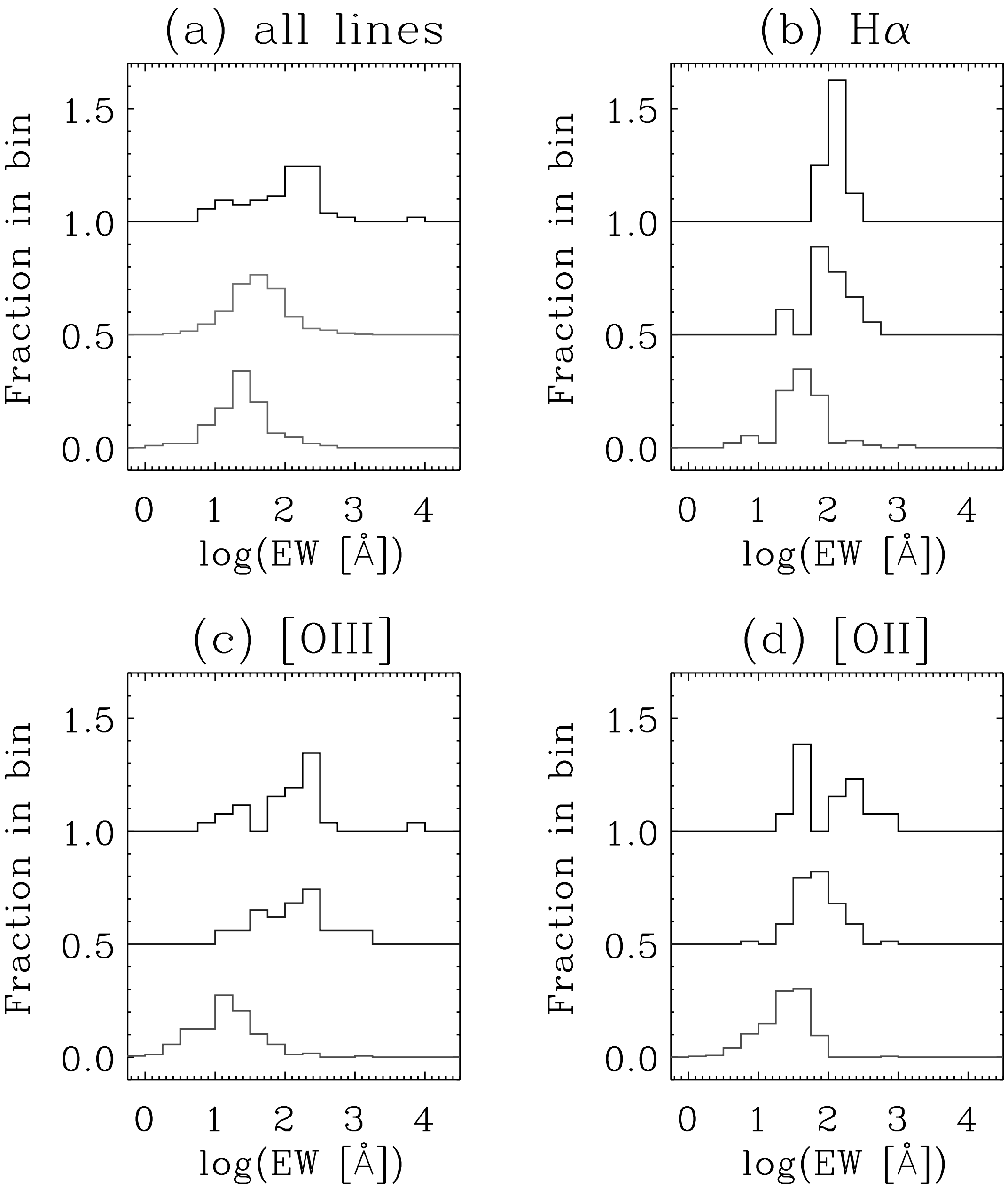

FIG. 7.—Histogram of rest-frame line equivalent widths. Histograms are normalized by the total sample size and offset vertically to ease comparison. In all cases our results are shown as the black line at top. In panel *a* we compare the widths of all lines with two local samples: the KISS red surveys (Salzer et al. 2001; Gronwall et al. 2004; *middle*), and the SINGG survey (Meurer et al. 2006; *bottom*). The remaining panels (*b–d*) split the sources by line identification, and our sample is compared to two surveys that extend out to moderate redshifts: the STIS Parallel Survey (Teplitz et al. 2003a), shown by the middle line, and the CFRS (Hammer et al. 1997), shown by the line at the bottom. [*See the electronic edition of the Journal for a color version of this figure.*]

Figure 8. The colors were chosen because they span the broadest λ coverage of the WFC filter set and because they do a reasonable job of separating sources by redshift. Only sources with $z_{\rm phot} < 1.62$ are included to limit the comparison sample to galaxies that would have [O II], or lines to the red, at measured $\lambda \leq$ 9750 Å where they could be detected with the grism. While there are very few ELGs in the red tail of the field-galaxy color distribution, the ELGs are not particularly blue. This can be seen in Table 4, which tabulates the median, first quartile, and third quartile colors of the two samples. The samples are subdivided by $z_{\rm phot}$ (field galaxies) and line identification (ELGs) so that colors at similar redshifts are compared. In general, ELGs do not show as much of a "red tail" to their color distributions but are otherwise similar to the general field population. This is seen by their third quartile colors, which are distinctly bluer for the ELGs compared to the field galaxies, while the first quartile and median colors are within ~0.2 mag of the field galaxies. There are two exceptions: the Hα emitters are somewhat redder than low-redshift field galaxies in $B_{435} - i_{775}$, and the [O II] emitters are distinctly bluer than the field galaxies, especially in $B_{435} - i_{775}$. We attribute the latter to the shift in λ_0 of the filters with redshift. At $z = 0.15, 0.53$, and 1.13 the $B_{435} - i_{775}$ color samples rest-frame colors $m_{378} - m_{674}$, $m_{284} - m_{507}$, and $m_{204} - m_{363}$;[10] hence, we are measuring rest-frame ultraviolet colors for the [O II] emitters, while the $B_{435} - i_{775}$ color for the other line emitters is still largely an optical color. Presumably the ELGs are mostly star-forming galaxies. This suggests that the

---

[10] The number in the subscript gives the approximate central λ in nanometers.

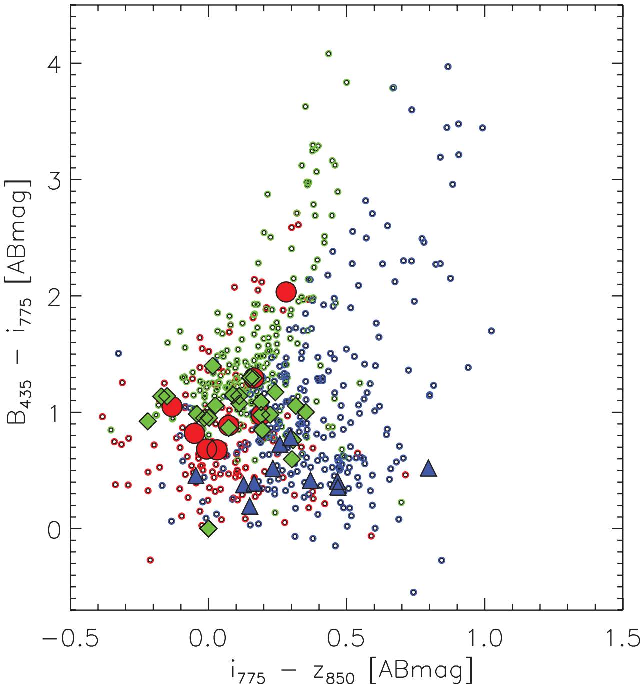

FIG. 8.—$B_{435} - i_{775}$ vs. $i_{775} - z_{850}$ two-color plot of sources in the HDF-N, using GOODS photometry (Giavalisco et al. 2004). Small circles are sources with $z_{\rm phot} \leq 1.62$ (C04), and filled symbols are ELGs identified in this study. The symbols are color-coded by $z_{\rm phot}$ and line identification, respectively, where red corresponds to $z_{\rm phot} < 0.30$ and Hα emitters (*circles*), green corresponds to $0.3 \leq z_{\rm phot} < 0.76$ and [O III] emitters (*diamonds*), and blue corresponds to $0.76 \leq z_{\rm phot} < 1.62$ and [O II] emitters (*triangles*).

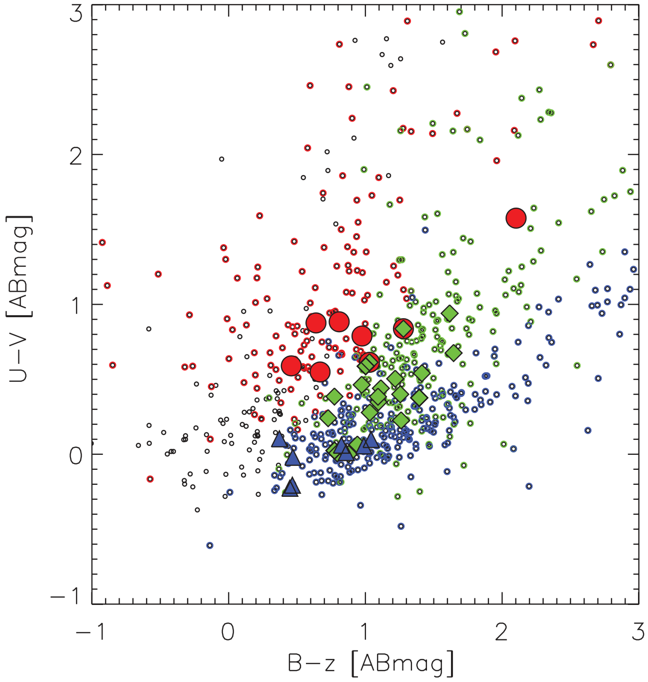

FIG. 9.—$(U - V)$ vs. $(B - z)$ photometry for sources in the HDF-N using the Hawaii group photometry (C04). The line identifications are fairly well sorted in this plane. The symbols used are the same as in Fig. 8.

rest-frame optical colors of ELGs are fairly normal, but the rest-frame UV colors are blue. This is reasonable and can be seen in the template spectra used in photometric redshift estimates. When normalized to unity at $\lambda = 4000$ Å there is relatively little variation in SED shape for $\lambda > 4000$ Å, but there are strong color variations with UV color getting bluer with later spectral type.

A better separation of the line emitters can be obtained by including broadband filters that extend further to the blue than WFC's filter set. Figure 9 shows that the $(U - V)$ versus $(B - z)$ diagram is particularly well suited for emission-line identification. We examined a variety of optical two-color diagrams and found this to be the best at discriminating between line emitters. If data in only three filters can be obtained, then the $(U - V)$ versus $(V - z)$ diagram also provides reasonable color separation between the emitters of the different lines.

5. LINE IDENTIFICATION AND REDSHIFT

Figure 10 compares the redshifts from the grism data with the spectroscopic redshift measurements from Cowie et al. (2004). Symbol shape and color are used to indicate the line identification, while filled and open symbols mark measurements with methods A and B, respectively. The dispersion in $z_{\rm grism} - z_{\rm spec}$ about the unity line is 0.016 for method A (15 measurements) and 0.009 for method B (20 measurements) after applying an iterative 3 σ rejection (one measurement was rejected in each case). We attribute the lower scatter from method B as reflecting its superior accuracy in measuring λ in off-center star formation knots.

The redshift accuracy depends on how secure the line identification is. For the relatively bright sources plotted in Figure 10, the identification can be considered secure in the cases where

TABLE 4
COLOR PROPERTIES OF HDF-N FIELD GALAXIES AND ELGS

	FIELD GALAXIES					EMISSION-LINE GALAXIES				
COLOR (1)	$z_{\rm phot}$ Range (2)	N (3)	25th (4)	Median (5)	75th (6)	Lines (7)	N (8)	25th (9)	Median (10)	75th (11)
$B_{435} - i_{775}$	<1.62	640	0.63	1.04	1.40	All	45	0.52	0.87	1.06
$B_{435} - i_{775}$	<0.30	145	0.44	0.70	1.04	Hα	8	0.79	0.93	1.11
$B_{435} - i_{775}$	0.30–0.76	243	1.07	1.27	1.67	[O III], Hβ	28	0.91	1.03	1.14
$B_{435} - i_{775}$	0.76–1.62	261	0.53	0.87	1.31	[O II]	13	0.39	0.46	0.73
$i_{775} - z_{850}$	<1.62	640	0.07	0.21	0.37	All	45	0.00	0.13	0.24
$i_{775} - z_{850}$	<0.30	145	−0.03	0.06	0.16	Hα	8	−0.02	0.05	0.17
$i_{775} - z_{850}$	0.30–0.76	243	0.06	0.17	0.27	[O III], Hβ	28	0.00	0.13	0.20
$i_{775} - z_{850}$	0.76–1.62	261	0.24	0.35	0.51	[O II]	13	0.13	0.23	0.37

NOTES.—Color statistics are given for two samples of galaxies in the HDF-N: field galaxies, selected purely by $z_{\rm phot}$ (C04), and ELGs selected from the grism data presented here. N (cols. [3] and [8]) gives the number of galaxies with GOODS photometry in each sample that match the $z_{\rm phot}$ criteria of col. (2) or contain the emission lines listed in col. (7). Cols. (4) and (9) give the first quartile color of the samples, cols. (5) and (10) list the median color, and cols. (6) and (11) list the third quartile color.

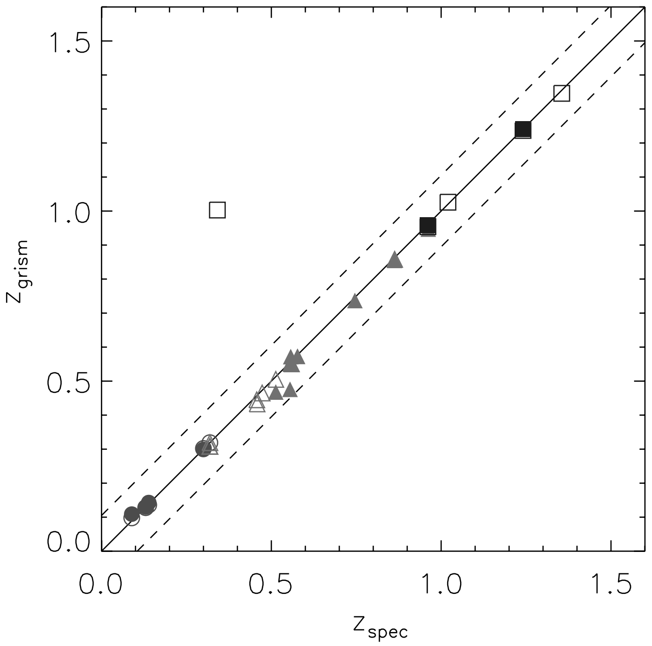

FIG. 10.—Comparison of spectroscopic redshifts from Cowie et al. (2004) and grism redshifts from this work. Measurements from method A are shown with filled symbols, and measurements from method B are shown as open symbols. The symbol shape and color indicate the grism line identification: Hα emitters are circles, [O III] emitters are triangles, and [O II] emitters are squares. The unity relationship is shown as a solid line; sources outside the dashed lines at $\Delta z = \pm 0.105$ are considered outliers. [*See the electronic edition of the Journal for a color version of this figure.*]

more than one line is identified or where the line is identified with Hα or [O II]. These two lines are relatively isolated, and usually there is no other plausible line within the redshift uncertainty of the first guess. In these cases, the dispersion in $z_{\rm grism} - z_{\rm spec}$ about the unity line is 0.010 for method A (10 measurements) and 0.007 for method B (13 measurements). The line identification is not secure if there is only one line, and we identify it as [O III]. The line could also be Hβ; however, by default [O III] is adopted as the identification under the assumption that typically the [O III] doublet is stronger than Hβ (cf. Hammer et al. 1997). There are five ELGs with spectroscopic z and single lines identified as [O III] in our data and found with method A, and six with method B; the dispersion of their residuals about the unity line is 0.025 and 0.009, respectively.

Single-line identification depends critically on the first-guess redshift. We find that in ~90% of the cases with both spectroscopic and photometric redshifts that $z_{\rm phot}$ is sufficiently accurate to get the correct line identification. Specifically, when $z_{\rm spec}$ is not employed as one of the redshift guesses 1 out of 16 of the method A line identifications changes, while 2 out of 20 of the method B identifications change. Of course, one also has to be careful with the spectroscopic redshifts; as noted by Lanzetta et al. (1998) the misidentification of spectroscopic sources previously had resulted in large discrepancies between $z_{\rm spec}$ and $z_{\rm phot}$ in the HDF-N. This is likely to be the case for ELG No. 37, which is the outlier in Figure 10. It has $z_{\rm spec} = 0.341$ in the Hawaii catalog, which would imply that we might see Hα at $\lambda = 8802$ Å or [O III] at $\lambda = 6657$ Å. No features are seen near either wavelength. Instead we see a strong line at $\lambda = 7467$ Å. This source has $z_{\rm phot} = 0.97$ from C04 and $z_{\rm phot} = 0.92$ from our own BPZ results. Using either of these produces a first-guess line identification as [O II] at $z_{\rm grism} = 1.00$, well within the expected redshift errors of both $z_{\rm phot}$ estimates.

The reliability of our $z_{\rm grism}$ estimates is similar to that seen for photometric redshifts, while the accuracy is much better. This can be seen by comparing photometric and spectroscopic redshifts (from Cowie et al. 2004) for the sources in the field. The dispersion about the unity line in $z_{\rm phot} - z_{\rm spec}$ is 0.073, 0.107, and 0.082 for $z_{\rm phot}$ estimates from C04, FLY99, and our BPZ results, respectively. Here we adopted a $|z_{\rm phot} - z_{\rm spec}| > 0.32$ rejection criterion and only considered sources with $z_{\rm spec} < 1.5$. The rejection criterion corresponds to 3 times the dispersion in $z_{\rm phot} - z_{\rm spec}$ from FLY99 calculated with a 3 σ clipping, while the $z_{\rm spec}$ limit is adopted to correspond to the observed $z_{\rm grism}$ range of our survey. The number of sources rejected/used in these calculations are 11/160, 3/103, and 12/107, respectively. Hence, ~5%–10% of photo-z estimates are significantly discrepant compared to $z_{\rm spec}$. This is similar to the reliability of our line identifications using $z_{\rm phot}$ as the first-guess redshifts. More importantly, the $z_{\rm grism}$ results are more accurate than $z_{\rm phot}$ (having a lower dispersion in $z - z_{\rm spec}$) by a factor of 5–12.

The above comparisons, of course, require a spectroscopic redshift. As illustrated in Figure 5, these correspond to the brighter galaxies. The mean i_{775} is 22.7 ABmag for the 22 ELGs we selected that also have $z_{\rm spec}$. The 24 ELGs without $z_{\rm spec}$ have a mean $i_{775} = 25.0$. For them the main reliability issue is the photometric error bars. The errors are typically larger for faint galaxies, and in six of these galaxies they translate into redshift errors large enough to allow alternate bright-line identifications. The choice of $z_{\rm phot}$ source can also be an issue. In eight cases the line identification changes depending on which first-guess redshift is used. In one galaxy without $z_{\rm spec}$, no line identifications are allowed in the range of allowed $z_{\rm phot}$ from our one estimate of $z_{\rm phot}$. There are a total of 14 cases that are ambiguous in one or more of these ways; 12 of those do not have a $z_{\rm spec}$ estimate. The i_{775} ABmag distribution of the sources with ambiguous line identification are marked in gray in the top panel of Figure 5, illustrating that the ambiguous identifications correspond to faint sources (mean $i_{775} = 25.46$ ABmag). These cases are identified in Table 2 with alternate line identifications noted in the Appendix. While some uncertainty remains for these objects, we emphasize that by selecting the line identification closest to the favored $z_{\rm phot}$ and prioritizing our $z_{\rm phot}$ sources, we increase the probability that we have picked the right line.

While one could hope that additional priors might remove the ambiguity of the line identifications, we have not found a satisfactory measurement to use. For example, Drozdovsky et al. (2005) decided on line ID, in part, by looking at the size of the host galaxies. However, size alone is not a great indicator of redshift. This is demonstrated in Figure 11, which shows the size versus redshift relationship of the objects in our field. There is little, if any, angular size evolution with redshift.

Correlations between the luminosity and line ratios have also been suggested to us for improving identifications. For example, the mass-metallicity relationship (Tremonti et al. 2004) is in the sense that galaxies with low mass, and hence low luminosity, have low metallicities, resulting in high excitations and thus typically higher [O III]/Hβ and [O III]/[O II] ratios; low-luminosity galaxies are more likely to be [O III] emitters, while high-luminosity galaxies are more likely to be [O II] emitters. However, on its own luminosity is unlikely to be useful in constraining identifications for (at least) three reasons. (1) Using G800L tends to select high-EW systems that are more likely to be high-excitation, low-metallicity systems; this should induce a bias toward [O III] emitters. The calibrating sample would need to have selection effects similar to the grism ELGs. (2) The mass-metallicity relationship is known to evolve with redshift (Savaglio et al. 2005); higher redshift galaxies of the same stellar mass have lower metallicities (again favoring [O III] emitters). (3) The luminosity-redshift relationship

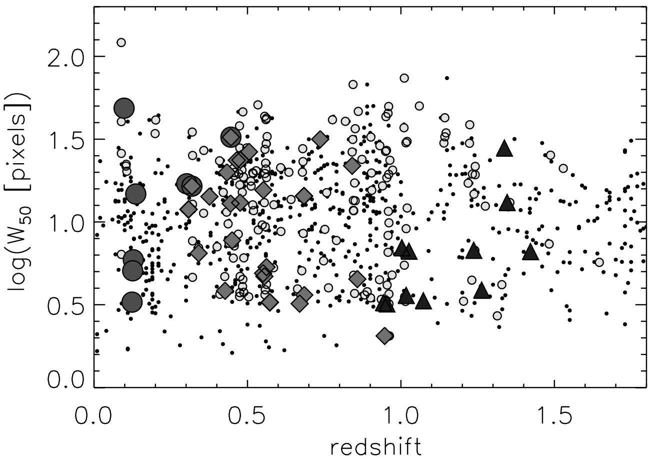

FIG. 11.—Angular size plotted against redshift for the sources in our field. Sources with photometric redshifts are plotted as small black dots. Small filled circles mark sources with spectroscopic redshifts. The large filled symbols mark the sources with grism redshifts; filled circles indicate Hα emitters, diamonds indicate [O III] or Hβ emitters, and triangles indicate [O II] emitters. [*See the electronic edition of the Journal for a color version of this figure.*]

goes in the wrong direction to remove the degeneracy. For example, ELG No. 45, one of the cases with ambiguous line identification, has $z_{\rm grism} = 1.422$ for our adopted [O II] identification, yielding $M_B = -21.3$, brighter than the local $M_B^\star$, which seems consistent with the [O II] identification. If we adopt the alternative [O III] identification then $z_{\rm grism} = 0.807$ and $M_B = -19.2$, much fainter than $M_B^\star$, which seems to be consistent with an [O III] identification. Either combination seems plausible, and the degeneracy is not broken.

One may also consider using EW as a prior to decide between possible line identifications, particularly in conjunction with luminosity. In the local universe it is very rare to have EW([O II]) > 100 Å; fewer than 2% of the prism-selected Hα ELGs in the sample of Gallego et al. (1996) meet this condition. Such EW values are more common from [O III] emission. When seen in [O II], the source typically has a low (fainter than $M_B^\star$) luminosity; $M_B \gtrsim -20$ (when converted to our adopted cosmology; Pérez-González et al. 2000; Gallego et al. 1996). Using EW as a prior would cast suspicion on the seven single-line [O II] galaxies in our sample with such high EW values. Such scrutiny is warranted since six of these seven have some ambiguity in the line identification (as noted in the Appendix); in four of those cases an [O III] identification is allowed depending on which $z_{\rm phot}$ is used as a first-guess redshift. If we were to use luminosity as well in the prior, changing the [O II] identification to [O III] in the ambiguous cases if EW([O II]) > 100 Å and $M_B < -20.0$, then two sources (Nos. 37 and 45) would be affected.

While the identifications of the high-EW [O II] emitters deserve some skepticism, at this time it would be inappropriate to apply an EW prior even in conjunction with luminosity. There are three reasons for this assessment. (1) As noted in § 4.2 the continuum levels used to determine EW are prone to large background subtraction uncertainties; hence, the accuracy of high-EW measurements are typically low. In this exploratory study we have not calculated the uncertainties in the continuum level that would need to be done to properly apply a prior. (2) High-EW([O II]) values have a precedent in the more distant universe: Hogg et al. (1998) found two [O II] emitters with EW > 100 Å, while there are 22 such sources in the SPS (Teplitz et al. 2003a, 2003b; these studies also note the problem in continuum determination). All these cases have $z_{\rm spec} \gtrsim 0.5$. We caution that the majority of the cases found by the SPS are also single-line sources, and thus one might also be suspicious of their proper identification. However, two of their high-EW [O II] emitters have additional lines that secure their identification. (3) Finally, we note that there is strong evidence for evolution in EW, with EW([O II]) increasing with redshift (especially for $z \gtrsim 0.9$), even for the most luminous galaxies (Hammer et al. 1997). Reasons (2) and (3) indicate that an EW prior based on the local universe may not be appropriate at the redshifts we are dealing with. We conclude that the high-EW([O II]) emitters need more scrutiny to confirm their reality. This should include a more careful determination of EW([O II]) using an improved error analysis, as well as follow-up spectroscopy to detect additional lines and confirm the line identification. If the high incidence rate of sources having EW([O II]) > 100 Å is confirmed, it would be further proof of strong redshift evolution in the star-forming properties of galaxies.

6. SUMMARY AND DISCUSSION

We have shown that a modest expenditure, three orbits, of ACS WFC grism time with the *HST* pointed at a "blank" high-latitude field results in the detection of dozens of ELGs out to $z \sim 1.5$. Here we found 46 ELGs in the HDF-N yielding a surface density of 3.9 ELGs arcmin^{-2}. The "blind" grism selection technique (method B) results in significantly more sources and better redshift accuracy. We attribute this to its ability to isolate individual emission-line knots within galaxies. The aXe selection technique (method A) relies on an initial catalog of sources, and hence is effectively a broadband (i.e., usually continuum) selection technique. While it often misses objects in which emission arises from a knot, it is adept at picking up line emission confined to a compact nucleus, which the "blind" technique can miss. Hence, the two techniques are complementary.

The ELGs found are most frequently [O III] (or Hβ) emitters at $z \sim 0.4$–0.9. Hα and [O II] emitters are also found, but are less common because of the smaller volume for the former and the limited depth of the observations for the latter. The ELGs represent a small fraction of the field population. There are 647 galaxies within the field of our observations having $z_{\rm phot} \leq 1.5$ in the C04 catalog, while 186 galaxies have spectroscopic $z \leq 1.5$ in the Cowie et al. (2004) compilation. While grism selection of ELGs does not result in a sample of the field that is in any way complete, the galaxies selected do have interesting properties. In particular, they tend to be low-luminosity high-EW systems. This suggests that they are experiencing an intense burst of star formation or may contain an AGN. A high [O III] EW suggests high excitation and low metallicity. Grism selection of ELGs may be a good means to locate the barely evolved building blocks of larger galaxies.

Our results are consistent with deeper G800L observations reported by the GRAPES team (Pirzkal et al. 2004; Xu et al. 2007) who obtained 92 ks of G800L observations of the HUDF (13 times longer than our HDF observations) split into five epochs. They found 113 ELGs in a field having similar area, using an algorithm equivalent to our method A (although differing in some details); 51 of these are brighter than our empirical line flux limit $F_{\rm line} = 3.0 \times 10^{-17}$ ergs cm^{-2} s^{-1}. This compares well with the 46 ELGs we find in the HDF. They also find [O III] sources to be the most frequently detected line, while the maximum $F_{\rm line}$ is 2.2×10^{-17} ergs cm^{-2} s^{-1} in the seven Lyα emitters they find, consistent with our nondetection of these sources.

Optimal use of grism data to discover ELGs requires additional data. This is because the grism spectra typically show only one emission line per object; hence, identification of the line from the low-resolution spectra is difficult, at least for the relatively short exposures used here. With longer exposures, often both the [O III] doublet and Hβ lines can be seen in ELGs having $z \approx 0.4$–0.9, hence the problem then becomes distinguishing between Hα and [O II] emitters.

The accuracy of the line identification can be improved if there is a good "first-guess" redshift for each source, either a spectroscopic redshift $z_{\rm spec}$ or a photometric redshift $z_{\rm phot}$. While the former produces the most accurate line identifications, there is typically little need for a grism spectrum of sources that already have a ground-based spectrum of sufficient S/N to determine a redshift. Use of $z_{\rm phot}$ as the first guess requires additional photometric data from *HST* or other sources to derive the redshift. Without these additional data, or follow-up spectroscopy, it may be impossible to identify the line and hence determine the redshift, which seriously diminishes the utility of the ELG discoveries. With a good $z_{\rm phot}$ first guess, lines can be identified with ~90% reliability, similar to the $z_{\rm phot}$ reliability but resulting in redshifts accurate to ~0.01 (3000 km $\rm s^{-1}$). This is about an order of magnitude better than $z_{\rm phot}$ estimates and is sufficient for separating ELG members of rich clusters from the field.

The requirement of additional photometry to obtain good emission-line redshifts amounts to a substantial additional investment of time and labor. In § 4.2 we examined color-color diagrams that are useful for sorting the ELGs by line identification. In general, filter combinations that span the full optical range seem to be the best suited for this purpose. The $U - V$ versus $B - z$ diagram provides the best discrimination, but requires wide-field *U*-band data that are hard to obtain from the ground and impossible to obtain with ACS and WFC. The $B_{435} - i_{775}$ versus $i_{775} - z_{850}$ diagram does a reasonable job at separating the [O II] emitters from the [O III] and Hα sources. Most of the discrimination comes from the $B_{435} - i_{775}$ color, which is the single color best suited for line discrimination from the ACS and WFC filter set. However, as shown in Figure 8, it does not discriminate well between Hα and [O III] emitters. For that, one needs to have a filter as far as possible toward short wavelengths so as to sample the rest-frame UV at modest redshifts. An efficient solution of this issue at *HST* resolution would require the installation of WFC3. Until then, terrestrial $(U - V)$ gives the best single color discriminator between line identifications.

The reliability of the line identification decreases with decreasing brightness, as the increasing photometric errors can result in ambiguous line identification. The investment of direct imaging time required to beat down the photometric redshift errors is larger than the time spent on the grism imaging; we spent three *HST* orbits imaging with G800L, while the GOODS direct images (B_{435} [3 orbits], V_{606} [2.5 orbits], i_{775} [2.5 orbits], z_{850} [5 orbits], at each pointing), as well as the original HDF images and ground-based imaging were used to determine the first-guess photometric redshifts. Even then, more than half of the ELGs we detected with $i_{775} > 24.5$ ABmag have some uncertainty in their line identification. Of particular concern are the faint [O II] identifications that have apparently large EW > 100 Å. These could signify strong redshift evolution in the star-forming population, as indicated by other studies (e.g., Hammer et al. 1997), or could be (in part) spurious due to contamination of misidentified [O III] emitters or large continuum-placement errors. The HDF-N is one of the best-studied deep fields, yet we still face these issues because of the faintness of the ELGs.

We conclude that ACS G800L grism data with minimal direct images provide a useful means of locating ELGs, but without additional data, they can provide only a limited interpretation of the nature of the sources. Photometric redshifts from broadband imaging can improve the reliability of line identifications. However, these data are also expensive to obtain, and the results are still likely to be ambiguous for the faintest ELGs we can detect. Secure redshifts for these still require ground-based spectroscopy. Fortunately, the line fluxes are easily within the reach of the current generation of 8 m class telescopes. For example, the Gemini Multi-Object Spectrographs can detect an emission line with a flux of 1.5×10^{-18} ergs $\rm cm^{-2}\ s^{-1}$ (one-tenth of our limiting line flux) and EW of 10 Å at S/N ~ 5 in a single 900 s exposure. An efficient strategy for finding and characterizing ELGs would then be to observe with ACS and the G800L grism to find the emission-line sources, employing broadband images (in, say, F814W and F606W) of a similar depth to locate the corresponding galaxy, then following up with ground-based spectroscopy to secure the redshift and identify additional lines.

ACS was developed under NASA contract NAS 5-32865, and this research has been supported by NASA grant NAG5-7697 and by an equipment grant from Sun Microsystems, Inc. The Space Telescope Science Institute is operated by Association of Universities for Research in Astronomy (AURA), Inc., under NASA contract NAS5-26555. We are grateful to K. Anderson, J. McCann, S. Busching, A. Framarini, S. Barkhouser, and T. Allen for their invaluable contributions to the ACS project at Johns Hopkins University. G. R. M. acknowledges useful conversations with Anna Pasquali, Marco Sirianni, James Rhoads, Sangeeta Malhotra, Chun Xu, and Søren Larsen. We thank the anonymous referee for suggestions that improved the science and readability of this paper.

APPENDIX

COMMENTS ON INDIVIDUAL SOURCES

Here we present notes on ELGs with multiple ELSs (lines and/or knots), those with striking morphologies, and cases where the line identification is in some way ambiguous. For each source we list the ELG ID number, the corresponding long name, and grism-redshift (in parenthesis).

1. *GOODSN J123641.63+621132.1* (*0.098*).—The lowest-redshift galaxy shows Hα emission from a bright knot, pinpointed with method B, 1.07″ to the east of the spiral galaxy core. This knot, combined with a fainter knot to the east of the core, results in a weak Hα detection with method A.

2. *GOODSN J123644.75+621157.4* (*0.124*).—The adopted identification of the single line in this source as Hα yields a redshift closest to the C04 $z_{\rm phot}$. However, the error bars in C04 and our $z_{\rm phot}$ also allow an identification of [O III], while the $z_{\rm phot}$ from FLY99 only allows [O III] as the identification.

3. *GOODSN J123633.16+621344.0* (*0.126*).—The adopted Hα line identification yields $z_{\rm grism}$ closest to $z_{\rm phot}$ from C04. However, the error bars from C04 also allow line identifications of [O III] or [O II], while our BPZ results allow Hα and [O III] as the line identification.

5. *GOODSN J123648.30+621426.9* (*0.136*).—Lopsided spiral, with a bright compact nucleus and bar. The spectrum extracted with method A shows weak Hα on top of a strong continuum. With method B, four Hα-emitting knots are identified with lines at a consistent λ (average $\lambda = 7456$ Å). A fifth ELS appears to have emission at a discrepant λ, perhaps due to misidentification of the emitting knot in the direct image.

7. *GOODSN J123658.06+621300.8* (*0.308*).—Inclined disk galaxy with a prominent knot offset by 0.35″. [O III] and Hβ emission arise from the galaxy nucleus.

8. *GOODSN J123626.57+621321.2* (*0.318*).—Our BPZ analysis provides the only $z_{\rm phot}$ source. The $z_{\rm phot}$ error bars allow the

single line to be identified as Hα, [O III], or [O II]. The adopted [O III] identification is closest to the third-strongest $z_{\rm phot}$ probability peak from BPZ.

9. *GOODSN J123650.82+621256.3* (*0.319*).—Edge-on disk galaxy with two emission-line knots separated by 0.96″ bracketing the nucleus. With method B, [O III] is clearly visible in both knots, and Hα is clearly detected in the southern knot, but is just below the detection limit in the northern knot. No emission lines are detected with method A, because the extracted spectrum does not fully contain the knots.

10. *GOODSN J123646.59+621157.5* (*0.341*).—The error bars on the C04 $z_{\rm phot}$ allow [O III] or [O II] as the line identification for the single detected line. The closest $z_{\rm grism}$ match is with [O III], which is also consistent with the FLY99 and BPZ $z_{\rm phot}$ analysis.

14. *GOODSN J123637.56+621240.4* (*0.445*).—This galaxy is apparently interacting with GOODSN J123637.64+621241.3, which we also detect as an ELG (see below). We find one line, [O III], with method B.

15. *GOODSN J123637.64+621241.3* (*0.446*).—The dominant system in the pair with No. 14. Method B detects two lines identified as [O III] and Hα, while only one low-EW line, [O III], is identified with method A.

17. *GOODSN J123657.30+621300.0* (*0.465*).—A barred spiral with arms forming a pseudoring. Line emission originates in an arm H II region about 1″ from the galaxy center.

20. *ACS J123636.58+621336.8* (*0.478*).—This source is not present in the GOODS-N r1.1z catalog, probably due to its faintness. Our own measurements of this source from data combining the GOODS images and other ACS images of the field yield photometry [B_{435}, V_{606}, i_{775}, z_{850}] = [28.16 ± 0.14, 27.69 ± 0.08, 26.77 ± 0.06, 27.72 ± 0.15] ABmag, while measurements from the C04 images yield [U, B, V, R, I] = [29.16 ± 0.55, 28.22 ± 0.30, 28.00 ± 0.28, 28.11 ± 0.34, 27.7 ± 0.6] ABmag and $z > 26$ ABmag (a nondetection). The relative brightness in i_{775} is likely due to the single bright line we observe at $\lambda = 7386$ Å whose flux (Table 2) is consistent with dominating i_{775}. Using this photometry, BPZ yields a best $z_{\rm phot} = 0.62$ consistent with the line being [O III]. However, a second peak in the probability distribution at $z_{\rm phot} = 0.1$ means that an identification as Hα cannot be ruled out. Because this source was not in the GOODS-N r1.1z catalog, it was excluded from the statistics given in Table 4.

22. *GOODSN J123655.58+621400.3* (*0.551*).—Emission corresponds to a knot above the plane of an edge-on disk galaxy.

24. *ACS J123657.48+621212.0* (*0.555*).—At first blush, this object appears to be the nucleus of a dwarf galaxy being shredded by an interaction with its neighbor GOODSN J123657.49+621211.2 projected 1.46″ toward the south-southeast. However, that source has $z_{\rm spec} = 0.669$ (C04). Our redshift is from a single line detected with both methods identified as [O III]. Even if the line were Hβ at $z = 0.600$, or Hγ at $z = 0.790$, the redshift would be significantly discrepant with its neighbor. Hence, the apparent interaction may be spurious and the sources an unrelated chance projection.

26. *GOODSN J123654.39+621434.7* (*0.573*).—The nucleus of this modestly inclined disk galaxy shows [O III] and Hβ. The emission lines are found with method A, not B, probably because the line emission is centered on the compact nucleus.

27. *GOODSN J123645.53+621330.2* (*0.670*).—The large error bars on the C04 $z_{\rm phot}$ allow the single line to be identified as Hα, [O III], or [O II]; the closest $z_{\rm grism}$ match is the adopted [O III] identification. This is consistent with the smaller error bars on the $z_{\rm phot}$ from BPZ, while none of the brightest likely lines match the $z_{\rm phot}$ from FLY99.

28. *GOODSN J123636.47+621419.1* (*0.684*).—The off-center knot in this small galaxy shows a broad, bright emission line well fit as [O III] blended with Hβ.

30. *GOODSN J123647.24+621134.7* (*0.717*).—BPZ is the only source of $z_{\rm phot}$ for this faint source, and yields allowed redshifts in the range $1 \lesssim z_{\rm phot} \lesssim 2$. However, none of the typical bright lines can match this range and the observed λ. The adopted [O II] identification corresponds to the line closest to the allowed range.

33. *GOODSN J123644.17+621430.5* (*0.858*).—The large C04 $z_{\rm phot}$ error bars for this source allow the single line to be identified as [O II], as well as the preferred [O III]. The $z_{\rm phot}$ from BPZ is consistent with our adopted [O III] line identification.

34. *GOODSN J123652.97+621257.1* (*0.943*).—The preferred $z_{\rm phot}$ from FLY99 identifies the single line as [O II], while the BPZ $z_{\rm phot}$ indicates the line may be [O III].

35. *GOODSN J123636.63+621347.1* (*0.947*).—This bright compact galaxy is detected in both Hβ and Hγ. It is the only Hγ source in the sample. The flux ratio $F_{{\rm H}\beta}/F_{{\rm H}\gamma} \sim 1.9$ is close to the expected case B ratio of 2.1 (for $n_e = 100$ cm^{-2} and $T_e = 10^4$ K; Dopita & Sutherland 2003). The lines are detected with method A but not with method B, probably because the line emission is centered on the compact nucleus. The case for interaction with GOODSN J123636.85+621346.2, a larger but slightly fainter lopsided spiral 1.81″ to the east-southeast, is strong since one of its spiral arms seems to be connected to GOODSN J123636.63+621347.1 in the high-pass filtered direct image, reminiscent of the M51/NGC 5194 system (see Fig. 2). However, the spectroscopic redshift of the spiral is significantly lower (0.846; C04) casting some doubt on this inference. The $z_{\rm phot}$ from C04 are consistent with these line identifications, while our BPZ $z_{\rm phot}$ is too low.

36. *GOODSN J123649.35+621155.4* (*0.954*).—Compact galaxy with two lines arising in the nucleus identified as [O II] and [Ne III] λ3869. The measured line ratio $F_{[{\rm Ne\,III}]}/F_{[{\rm O\,II}]} \sim 0.38$ indicates a high excitation; it corresponds to the 80th percentile in this ratio for the local ELGs that display both lines in the catalog of Terlevich et al. (1991).

37. *GOODSN J123649.47+621456.9* (*1.003*).—This source has the largest discrepancy between $z_{\rm spec}$ and $z_{\rm grism}$ in Figure 10. The original source for the reported $z_{\rm spec} = 0.341$ is Cohen et al. (2000) where the spectrum is given a quality code of 5: "one emission line only, reality uncertain, assume 3727 Å" (Cohen et al. 1999); that is, a single weak line in the spectrum. Both our BPZ results and those of C04 indicate very similar $z_{\rm phot}$: 0.921 and 0.970, respectively. While there is no good match at $z \approx 0.34$ for the line we detect at $\lambda = 7469$ Å, adopting either $z_{\rm phot}$ estimate for our first-guess redshift identifies the line as [O II] at our adopted $z_{\rm grism} = 1.003$. Using this redshift, then the line found by Cohen et al. (2000) may be [O II] λ2470 or [Ne IV] λ2423, if the weak line they found is real.

40. *GOODSN J123645.46+621357.3* (*1.073*).—The preferred $z_{\rm phot}$ from FLY99 yields the single-line identification of [O II], while the BPZ $z_{\rm phot}$ indicates that the line may be [O III].

42. *GOODSN J123653.51+621141.4* (*1.263*).—The C04 $z_{\rm phot}$ yields our adopted [O II] line identification. The $z_{\rm phot}$ from BPZ is lower and outside the C04 error bars, but does not allow any of the standard bright line guesses to correspond with the observed line λ.

44. *GOODSN J123652.77+621354.7* (*1.346*).—The brightest knot of this chain galaxy has one line identified as [O II].

45. *GOODSN J123642.55+621150.3* (*1.422*).—The adopted [O II] identification for the single line of this source is consistent with $z_{\rm phot}$ from C04 and FLY99, while BPZ prefers a lower $z_{\rm phot}$ consistent with an [O III] identification.

46. *GOODSN J123648.48+621120.7* (*1.424*).—BPZ is the only $z_{\rm phot}$ source for this faint source; the error bars allow an [O III] identification, as well as the adopted [O II].

REFERENCES

Abraham, R. G., et al. 2004, AJ, 127, 2455

Beckwith, S. V. W., et al. 2006, AJ, 132, 1729

Benítez, N. 2000, ApJ, 536, 571

Benítez, N., et al. 2004, ApJS, 150, 1

Bertin, E., & Arnouts, S. 1996, A&AS, 117, 393

Blakeslee, J. P., Anderson, K. R., Meurer, G. R., Benitez, N., & Magee, D. 2003a, in ASP Conf. Ser. 295, Astronomical Data Analysis Software and Systems XII, ed. H. E. Payne, R. I. Jedrzejewski, & R. N. Hook (San Francisco: ASP), 257

Blakeslee, J. P., et al. 2003b, ApJ, 589, 693

Blanton, M. R., et al. 2003, ApJ, 592, 819

Bohlin, R. C., Hartig, G., & Martel, A. 2001, HRC and WFC Flat-Fields: Standard Filters, Polarizers, and Coronograph, Instrument Science Report ACS 2001-11 (Baltimore: STScI)

Bouwens, R. J., Illingworth, G. D., Blakeslee, J. P., & Franx, M. 2006, ApJ, 653, 53

Capak, P. L. 2004, Ph.D. thesis, Univ. Hawaii (C04)

Carroll, S. M., Press, W. H., & Turner, E. L. 1992, ARA&A, 30, 499

Coe, D., Benítez, N., Sánchez, S. F., Jee, M., Bouwens, R., & Ford, H. 2006, AJ, 132, 926

Cohen, J. G., Hogg, D. W., Blandford, R., Cowie, L. L., Hu, E., Songaila, A., Shopbell, P., & Richberg, K. 2000, ApJ, 538, 29

Cohen, J. G., Hogg, D. W., Pahre, M. A., Blandford, R., Shopbell, P. L., & Richberg, K. 1999, ApJS, 120, 171

Cowie, L. L., Barger, A. J., Hu, E. M., Capak, P., & Songaila, A. 2004, AJ, 127, 3137

Dahlen, T., Mobasher, B., Somerville, R. S., Moustakas, L. A., Dickinson, M., Ferguson, H. C., & Giavalisco, M. 2005, ApJ, 631, 126

Dickinson, M. 1998, in The Hubble Deep Field, ed. M. Livio, S. M. Fall, & P. Madau (New York: Cambridge Univ. Press), 215

Dopita, M. A., & Sutherland, R. S. 2003, Astrophysics of the Diffuse Universe (Berlin: Springer)

Drozdovsky, I., Yan, L. Chen, H.-W., Stern, D., Kennicutt, R., Jr., Spinrad, H., & Dawson, S. 2005, AJ, 130, 1324

Fernández-Soto, A., Lanzetta, K. M., & Yahil, A. 1999, ApJ, 513, 34 (FLY99)

Gallego, J., Zamorano, J., Rego, M., Alonso, O., & Vitores, A. G. 1996, A&AS, 120, 323

Giavalisco, M., et al. 2004, ApJ, 600, L93

Gronwall, C., Salzer, J. J., Sarajedini, V. L., Jangren, A., Chomiuk, L., Moody, J. W., Frattare, L., & Boroson, T. A. 2004, AJ, 127, 1943

Hack, W. J. 1999, CALACS Operation and Implementation, Instrument Science Report ACS-99-03 (Baltimore: STScI)

Hammer, F., et al. 1997, ApJ, 481, 49

Hogg, D. W., Cohen, J. G., Blandford, R., & Pahre, M. A. 1998, ApJ, 504, 622

Hook, R. N., & Fruchter, A. S. 1997, in ASP Conf. Ser. 125, Astronomical Data Analysis Software and Systems VI, ed. G. Hunt & H. E. Payne (San Francisco: ASP), 147

Kashikawa, N., et al. 2006, ApJ, 648, 7

Kodaira, K., et al. 2003, PASJ, 55, L17

Koekemoer, A. M., Fruchter, A. S., Hook, R. N., & Hack, W. 2002, in The 2002 *HST* Calibration Workshop: Hubble after the Installation of the ACS and the NICMOS Cooling System, ed. S. Arribas, A. Koekemoer, & B. Whitmore (Baltimore: STScI), 339

Lanzetta, K. M., Fernández-Soto, A., & Yahil, A. 1998, in The Hubble Deep Field, ed. M. Livio, S. M. Fall, & P. Madau (New York: Cambridge Univ. Press), 143

Le Fèvre, O., Crampton, D., Lilly, S. J., Hammer, F., & Tresse, L. 1995, ApJ, 455, 60

Madgwick, D. S., et al. 2002, MNRAS, 333, 133

Mei, S., et al. 2005, ApJS, 156, 113

Meurer, G. R. 2006, in The 2005 *HST* Calibration Workshop: Hubble after the Transition to Two-Gyro Mode, ed. A. M. Koekemoer, P. Goodfrooij, & L. L. Dressel (Greenbelt: NASA), 95

Meurer, G. R., et al. 2002, in The 2002 *HST* Calibration Workshop: Hubble after the Installation of the ACS and the NICMOS Cooling System, ed. S. Arribas, A. Koekemoer, & B. Whitmore (Baltimore: STScI), 65

———. 2006, ApJS, 165, 307

Osterbrock, D. E. 1989, Astrophysics of Gaseous Nebulae and Active Galactic Nuclei (Mill Valley: University Science)

Pasquali, A., Pirzkal, N., & Walsh, J. R. 2003, The In-Orbit Calibration of the WFC G800L Grism, ST-ECF Instrument Science Report ACS 2003 (Garching: ST-ECF)

Pérez-González, P. G., Zamorano, J., Gallego, J., & Gil de Paz, A. 2000, A&AS, 141, 409

Pirzkal, N., Pasquali, A., & Demleitner, M. 2001, ST-ECF Newsletter, No. 29, 5

Pirzkal, N., et al. 2004, ApJS, 154, 501

———. 2006, ApJ, 636, 582

Salzer, J. J., et al. 2001, AJ, 121, 66

Savaglio, S., et al. 2005, ApJ, 635, 260

Taniguchi, Y., et al. 2005, PASJ, 57, 165

Teplitz, H. I., Collins, N. R., Gardner, J. P., Hill, R. S., Heap, S. R., Lindler, D. J., Rhodes, J., & Woodgate, B. E. 2003, ApJS, 146, 209

Teplitz, H. I., Collins, N. R., Gardner, J. P., Hill, R. S., & Rhodes, J. 2003, ApJ, 589, 704

Terlevich, R., Melnick, J., Masegosa, J., Moles, M., & Copetti, M. V. F. 1991, A&AS, 91, 285

Tremonti, C. A., et al. 2004, ApJ, 613, 898

Walsh, J. R., & Pirzkal, N. 2005, Flat-Field and Sensitivity Calibration for ACS G800L Slitless Spectroscopy Modes, Instrument Science Report ACS-05-02 (Baltimore: STScI)

Williams, R. E., et al. 1996, AJ, 112, 1335

Xu, C., et al. 2007, AJ, in press (astro-ph/0701875)